Babeş-Bolyai University
Cluj-Napoca
Doctoral School of Physics

University of Agricultural Sciences and Veterinary Medicine Cluj-Napoca
Doctoral School of Veterinary Medicine

RADU ANGELIN MARIAN POPESCU

IN VITRO AND *IN VIVO* OPTIMIZATION STUDIES OF BIOACTIVE SILICATE MATERIALS FOR TISSUE ENGINEERING APPLICATIONS

- DOCTORAL THESIS SUMMARY -

SCIENTIFIC COORDINATORS:
ASSOC. PROF. DR. HABIL. LUCIAN BAIA
PROF. DR. IONEL PAPUC

CLUJ-NAPOCA
-2017-

Table of Contents

INTRODUCTION

Millions of patients worldwide suffer significant bone loss each year due to various diseases, trauma or congenital illnesses, most often leading to premature disabilities and reduced quality of life for the sick [1–3]. Approximately 500,000 bone graft surgical interventions are performed annually in the United States and over 2.3 million worldwide, mainly for repairing defects in orthopedics, cranio-maxillo-facial surgery and neurosurgery [3,4]. These figures will increase exponentially in the next 10 to 15 years due to the doubling of the US population aged over 65 [5] and the increase in life expectancy of the world's population.

Bone tissue engineering focuses on regeneration processes of natural tissue. The bone, a well-vascular complex, indicates that the engineering of this tissue is an interdisciplinary domain based on the combination of three main components: cells, signaling molecules, and a macroporous artificial structure (macroscopic support or scaffold) acting as a temporary support for cell proliferation. Scaffolds mimic the extracellular matrix and must provide adequate mechanical properties and porosity to allow tissue growth [6]. Ideally, the created material should not only possess osteoconductivity but also osteoinductivity and must be biodegradable.

This thesis is structured in 9 chapters, along with the related subchapters. The first two chapters represent the current state of knowledge in the field of the topic, fragments that seek to highlight the particular importance of creating and applying viable bioactive structures, with the ultimate aim of faster and more efficient cure of lesioned tissue. The results section contains 4 distinct studies, which clearly defines the purpose of this paper, while the conclusions and perspectives chapter detail the shortcomings encountered and the need for an evolution in the forthcoming projects.

1. FUNDAMENTAL ELEMENTS OF OSTEOLOGY

Structural, compact bone is a dense and complex material that is delineated by basic units called osteons. Each osteon comprises the concentric bone lamellae surrounding a central canal called the Haversian canal [7,8]. The bone lashes are made up of a matrix (organic and mineral) and specialized cells called osteocytes. This matrix is composed of collagen fibers, calcium phosphate crystals and a fundamental substance mainly containing mucopolysaccharides [9,10]. The bone in different parts of the skeleton differs in terms of the proportion and layout of collagen, calcium phosphate, and basic cement, thus distinguishing two types of bone such as the spongy (trabecular) bone and the compact bone [11]. The bone is considered a very specialized connective tissue formed on the basis of less specialized tissues through a process called ossification, osteogenesis or more simplified bone formation [10]. During the bone formation some modified connective tissue cells called osteoblasts produce an amorphous starting material, later on becoming dense and fibrous, and is being called osteoid. Calcium phosphate crystals are then deposited in the osteoid, transforming it into a matrix [9,11]. Osteoblasts tend to be trapped in their own secretion and as the matrix strengthens around them, they become osteocytes.

2. BIOMATERIALS IN BONE TISSUE ENGINEERING

Millions of orthopedic prostheses made from biomaterials have been implanted with a lifetime guarantee of about 15 years in 75 to 85% of cases. Improved metal alloys (titanium, stainless steel 316L, 420, 440), high-level polymers and ceramics (ZrO_2, Al_2O_3) are the reason these successful medical tools have improved the quality of life of millions of patients worldwide [12–17]. However, an accelerated increase in life expectancy among the global population requires a period of operation of such medical devices more than 30 years [14,18]. Thus, in order to meet this need, a change of direction was proposed, which supposes the regeneration of lesioned tissues in exchange for replacing them with inert substitutes. Such a change, from a material-biomechanical approach to a biological tissue regeneration, requires a much deeper understanding of molecular biology [19]. In the current clinical use, three categories of materials are described as follows: resorbable, bioactive and inert.

The biological response to a sol-gel synthesized bioactive glass of formula CaO-P_2O_5-SiO_2 provides evidence that bone regeneration is possible. Biological molecules can exchange with the hydrated layers of porous material, maintaining their conformation and biological activity [17,20–22].

The approach to nanotechnology in medical engineering was proposed for a wide range of biomedical applications, using the term nanomedicine. Nanoscience and nanotechnology are two attractive concepts in relation to regenerative medicine and tissue engineering since, in the first instance, the cell-biomaterial interaction is carried out at the nano level (eg <100 nm) [23]. At the nanoscale, the properties that determine cell-biomaterial type interactions, such as the specific surface, porosity, hydrophilicity and wettability, properties that influence cell adhesion and provide fusion with the host tissue are fundamentally different from those on a micrometric scale [24,25].

For bone tissue, fusion with bioactive glass occurs due to the biological equivalence between the bone mineral component and the HAC layer formed on the surface of the material [26]. With regard to soft tissue, collagen fibers are chemoresorbed by the SiO_2-rich porous layer, by electrostatic forces, ionic interactions or hydrogen bonds. In this case HA is precipitated and crystallized on the collagen fibers and on the surface of the glass [27].

The term scaffold defines a structurally synthesized structure (macroscopic support) in order to support and promote physiological tissue regeneration. In general, scaffolds are designed for use in bone tissue engineering. Such structures are typically made of degradable, porous materials that can provide the necessary mechanical support during the repair and regeneration of the affected bone [28,29].

In the case of bioactive scaffolds, it is necessary to control the solubility of the material. A low solubility material is required if the scaffold is designed to last for a long time. A controlled dissolution rate is indispensable when synthesizing a scaffold for bone augmentation with a material such as 45S5 Bioglass® [18,30]. Therefore, a fundamental understanding of the factors that influence solubility and bioreactivity is a key element for the development of new materials that can improve tissue regeneration *in situ* [31–33].

The limitations of conventional methods have led to the use of rapid prototyping technology (RP), to improve the original model and to manufacture 3D scaffolding with

interconnected porous networks. In recent years, computerized hierarchy techniques (CTD and SFF) have allowed the design of anatomical structures with a porous architecture that can maintain the balance between functions and mechanical strength. Such methods have facilitated the manufacture of controlled scaffolds, polymers, hydrogels, ceramics and even biocompatible metals [34].

Therefore, the major challenge in developing a scaffold lies primarily in the choice of a suitable combination of biomaterials with a required bag of properties. This field is still open to new ideas and attempts to create the most appropriate structure that contains the whole palette of features indispensable to effective tissue replacement *in vivo*.

Materials Selection

- **Silver**

This element, in moderate concentrations, is well known for its antimicrobial qualities against a broad spectrum of Gram positive and Gram negative bacteria, fungus, protozoa and certain types of viruses [35,36]. Silver is also effective against resistant strains and bacteria involved in in-hospital, postoperative infections [37,38]. This metal, with its well-known antiseptic properties, has been used over time to manufacture large varieties of materials such as bioactive glasses, titanium alloys and polymers [36,39,40].

- **Gold**

Gold, the metal considered the most precious of many ancient civilizations, has also taken place in medical procedures, from ancient times to the present, conquering many fields ranging from the pharmaceutical industry to the oncology industry [41,42].

Although gold is a noble metal and a material often used because of its resistance to oxidation, its physical, optical, magnetic and electrical properties, it can form a multitude of other compounds. The oxidation states of gold in its various compounds vary from -1 to +5, but Au (I) and Au (III) are dominant.

Gold nanoparticles have proven to be attractive materials for applications in biology and medicine, mainly due to their physical and chemical properties. As an adjunct in tissue engineering, gold and AuNP play an important role in potentiating or even adding new features to tissue regeneration materials [43]. Thus, these nanostructures are currently considered the most stable metal NP [44,45].

- **Copper**

Similar to silver, copper is also used for thousands of years in areas such as food and medicine. Numerous studies suggest that by introducing Cu^{2+} ions into a bioactive matrix it is possible to improve angiogenesis by stabilizing the expression of the induction factor of hypoxia (HIF-1α) [46]. This factor plays an extremely important role both in cell recruitment and differentiation, as well as in the formation of blood vessels [47,48]. Copper is an essential co-factor, an activator of a significant number of proteins, but its homeostasis must be closely controlled [49]. Excessive or malfunctioning of this element may result in a particular cellular toxicity due to accidental redox reactions, catalysed by free copper [50].

Copper ions have been reported to be the most active species in terms of antibacterial action [51,52]. Repeated contact with bacteria or cells is due to the migration of Cu^{2+} to the environment [53].

- **Sodium Alginate**

Alginate is a biopolymer found in marine algae, especially in brown algae (*Phaeophyceae*) [54]. It is extracted from the seaweed cell wall by treatment with alkaline aqueous solutions, frequently with NaOH. The extract is filtered and then, in the presence of certain divalent cations (Ca^{2+}, Sr^{2+}, Ba^{2+}), the alginate precipitates. After purification, water-soluble sodium alginate is obtained [55–57].

Alginate has been active for decades in the food industry and in recent years as a basic material in tissue engineering [54]. Lately, this natural polymer is considered by the researchers to be one of the most desirable materials for the formation of composite scaffolds, due to the fulfillment of all of the above-mentioned characteristics, plus it is also non-immunogenic, a particularly important property when taken in calculate its activity *in vivo* [54,55]. However, the alginate also has several disadvantages such as deficient enzyme degradation in the mammalian organism and natural cellular nonadhesion [58,59]. Over the last decade, these drawbacks have been studied to overcome, helping to leverage far more intense alginate hydrogels [60].

- **Pullulan**

Pullulan is a naturally occurring, linear and unbranched polymer (exopolysaccharide) produced mainly by *Aureobasidium Pullulans* [61]. The structure of this compound mainly consists of α-1,6 maltotriose (G3) (Fig. 2.4.4.1). These G3 repeat units contain two glycosidic α-1,4 bonds [62]. Pullulan contains nine hydroxyl groups on each repeating unit in its structure, any one of which can be easily replaced by another chemical group to enhance its surface properties [63,64]. The excellent mechanical properties of this exopolysaccharide along with biocompatibility, hemocompatibility, hydrophilicity, non-mutagenicity and non-toxicity make it a promising material in tissue engineering [65–68]. The only limitation of this polymer is its inability to provide a surface that cells adhere to and proliferate naturally and efficiently [69]. However, this shortcoming has been overcome by various HA surface deposition techniques, the incorporation into the structure of small functional groups (arginine-glycine-aspartate) or combination with recognized cell polymers (gelatin, collagen) [70–73].

The purpose of the thesis

The main purpose of this PhD thesis was the design of a material which, on the one hand, meets the basic criteria in the literature on structure, bioactivity and biocompatibility, and on the other hand, succeed in completing some of the shortcomings present at the time in the engineering of bone tissue.

3. SYNTHESIS METHODS

3.1 Sol-Gel Synthesis

The precursors used in the synthesis of the first two compositions were tetraethylortosilicate (TEOS), triethylphosphate (TEP), calcium nitrate tetrahydrate ($Ca(NO_3)_2 \times 4H_2O$), copper nitrate trihydrate ($Cu(NO_3) \times 3H_2O$) and silver nitrate ($AgNO_3$). The hydrolysis was carried out in the presence of nitric acid (HNO3) and the molar ratio between ($HNO_3 + H_2O$) / (TEOS + TEP) was equal to 8. Stabilization of the samples was carried out by heat treatment at a temperature of 600 ° C.

3.2 Synthesis of gold nanoparticles and their stabilization with Pluronic F-127

AuNP were synthesized by the Turkevich-Frens method [74]. Briefly, the chloroauric acid was dissolved in ultra-pure water to a concentration of 10^{-3}M solution, and then the solution was brought to boiling under continuous stirring. Then, 38.8×10^{-3} trisodium citrate was added rapidly to the solution in a volume ratio of 10:1. The boiling and shaking processes then continued for another 30 minutes, and then the colloid was cooled to room temperature. The obtained AuNPs were stabilized with Pluronic F127 by simply mixing the colloidal solution with the polymer solution to a final concentration of 0.5×10^{-3} M.

3.3 Scaffold Synthesis

The PVA polymer was dissolved in ultra-pure water. Subsequently, in the obtained solution, the silica matrix (SiO_2-CaO-P_2O_5) was added. The obtained mixture was immersed for a few minutes by cubic pieces of polymeric sponge, 1 cm in diameter. These molds were then dried at 60°C for 4 hours and then the dipping procedure was repeated to produce a double coating. Finally, the samples obtained were dried at 60°C for 24 hours. The heat treatment scheme assumed a total period of 16 hours.

3.4 Synthesis of the composite material

To obtain the polymer solution with a final concentration of 4% (w/v), the two polymers were dissolved in ultra-pure water at a temperature of 80°C with continuous stirring. The bioactive material was added to the obtained mixture until a concentration of 0.5% glass was obtained [75,76]. The composite solution was dropped in a solution of 4% calcium chloride to produce capsules of ~ 2-3 mm in diameter.

4. INVESTIGATION METHODS

4.1 Structural and morphological investigation methods

4.1.1 ***X-Ray diffraction (XRD)***
4.1.2 ***Infrared absorption spectroscopy (FT-IR)***
4.1.3 ***Ultraviolet and visible spectrometry (UV-Vis)***
4.1.4 ***Scanning electron microscopy (SEM)***
4.1.5 ***X-ray Dispersive Spectrometry (EDX)***
4.1.6 ***Transmission electron microscopy (TEM)***
4.1.7 ***Paramagnetic / spin electron resonance (EPR)***
4.1.8 ***X-ray Photoelectronic Spectroscopy (XPS)***
4.1.9 ***Specific area and pore volume***
4.1.10 ***Plasma inductively coupled plasma spectrometry (ICP-Q-MS)***
4.1.11 ***Fluorescence spectroscopy***

4.2 *In vitro tests*

4.2.1 ***Bioactivity***
4.2.2 ***Biocompatibility***
4.2.3 ***Ionic release***
4.2.4 ***Antibacterian activity***
4.2.5 ***Cell viability***
4.2.6 ***Sample sterilization***

4.3 *In vivo tests*

4.3.1 ***Selection of biological material***
4.3.2 ***Surgical Procedures***
4.3.3 ***Dosage of serum osteocalcin***
4.3.4 ***Pain management***
4.3.5 ***Medical imaging***
4.3.6 ***Digital photography***
4.3.7 ***Necropsic method***
4.3.8 ***Histological Method***

5. SYNTHESIS AND CHARACTERIZATION OF SILICATE GLASSES DOPED WITH DIFFERENT CONCENTRATIONS OF SILVER OXIDE FOR THEIR USE IN BONE TISSUE ENGINEERING

5.1 Results and discussions

5.1.1 Structural characterization

Reflections obtained by XRD measurements on samples subjected to thermal stabilization treatment reveal a predominantly amorphous structure (Fig. 5.1.1.1 **a**). However, around 2θ ~ 32 ° one can be observed some signals associated with crystallisation centers, specific values, suggesting the formation of the tricalcium phosphate phase, encountered as $Ca_3(PO_4)_2 \cdot H_2O$ [77]. In the overlapping FT-IR spectra of the five compositions, we can see absorption bands characteristic of stretching and bending vibrations of the groups Si-O-Si (1040 și 860 cm^{-1}), (510 cm^{-1}) (Fig. 5.1.1.1 **b**). The water is present through the broad signal around 1640 cm^{-1}. The 1440 cm^{-1} band indicates the presence of the carbonate group, and the 560 and 580 cm^{-1} signals indicate the presence of phosphate groups [77].

The superposed UV-Vis spectra express between 300 and 330 nm a signal arising from the electronic transition in metallic Ag (Fig. 5.1.1.1 **c**) [78]. This signal increases in intensity with the increase of silver oxide added [79]. According to the literature, Ag doped samples can reveal surface plasmon resonance bands in the range of 400-500 nm as a consequence of the presence of AgNP [78,79]. Through the detailed analysis of our spectra, an absorption signal can be observed with a peak around 420 nm (Fig. 5.1.1.1 **c**). This signal is most intense at the sample with x = 0.5 mol% Ag_2O and is associated with the existence of AgNP in the silica matrix [79]. The band shape is asymmetric due to another signal of surface plasmon resonances of AgNP agglomerations, which overlaps the signal given by the resonances of the isolated plasmids of isolated AgNP. With the increase in silver concentration, a slight movement of the band from 420 nm to 450 nm can be observed as a consequence either of multiplication of cluster aggomerations or increase in size [78,79].

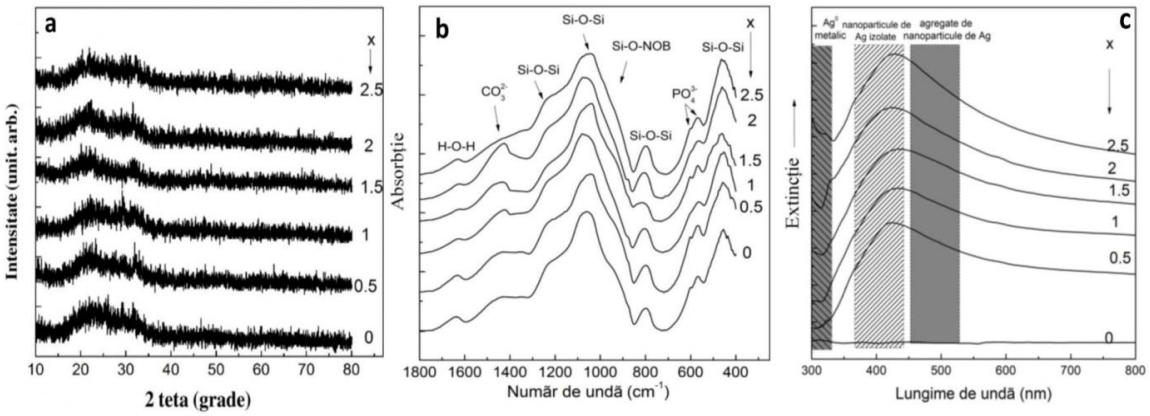

Fig. 5.1.1.1 XRD measurements (a), FT-IR spectra (b) and UV-vis spectra (c) obtained on the system samples $60SiO_2 \cdot (32\text{-}x)CaO \cdot 8P_2O_5 \cdot xAg_2O$(mol%).

5.1.2 Bioactivity testing

After immersing for 7 days in SBF, the sample diffractograms indicate the HA phase as evidenced by the signals recorded at 2θ ~ 26 ° and 32 ° (Fig. 5.1.2.1 **a**). Also, specific signals for silver chloride (AgCl) can be observed at 2θ ~ 46 °. In order to make it easy to associate the apatite phase and the silver chloride, the diffractograms of the two structures were added as the references [80]. According to the literature, silver chloride in small amounts has no negative effects on the biological environment, moreover it is preferred to the detriment of a high concentration of silver nanoparticles [81].

In the FT-IR spectra of samples immersed in SBF for 7 days, the bands at the 604 and 564 cm^{-1} values show a similar intensity at all concentrations (Fig. 5.1.2.1 **b**). This indicates good bioactivity for all samples [77]. However, the sample containing 0.5 mol% of Ag_2O shows the highest potential for bioactivity, also considering that it has a weak silver chloride signal.

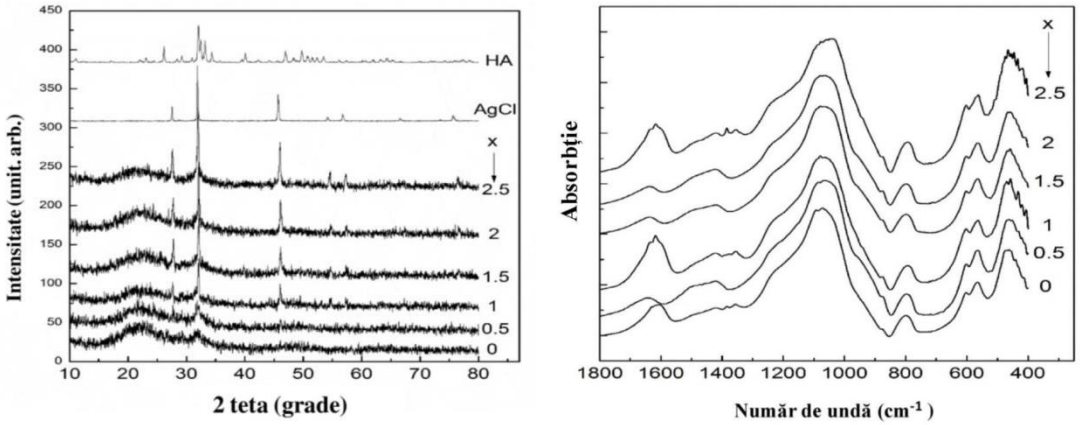

Fig. 5.1.2.1 Diffractograms (a) and FT-IR spectra (b) of the samples in the system $60SiO_2 \cdot (32\text{-}x)CaO \cdot 8P_2O_5 \cdot xAg_2O$(mol%), after immersion in SBF for 7 days.

5.1.3 Cell viability

Viability for all samples is around 100%, suggesting good compatibility with living tissues. The best evolution is the sample with 0.5 mol% Ag_2O, which shows an increase in cellular proliferation along the three concentrations used (75, 150 și 300 μg/ml) (Fig. 5.1.3.1).

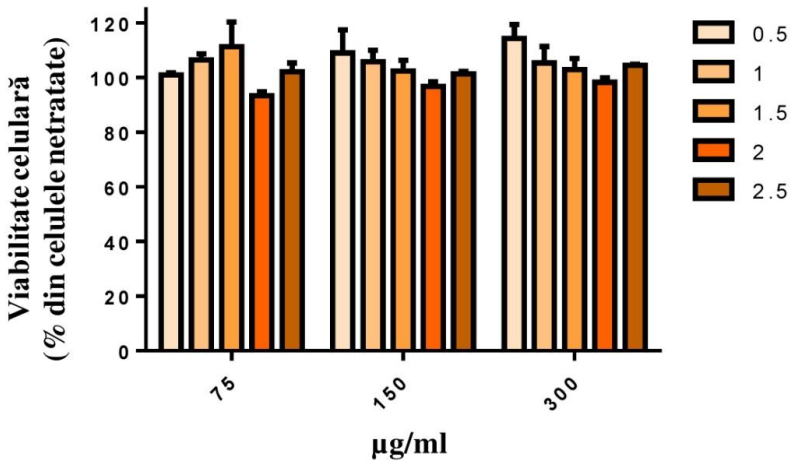

Fig. 5.1.3.1 Diagram of cell viability of samples in the system $60SiO_2 \cdot (32\text{-}x)CaO \cdot 8P_2O_5 \cdot xAg_2O$(mol%)

5.1.4 Testing of cell proliferation after inclusion of the bioactive material in a polymeric structure

Glasses obtained from structural optimization were included in a polymeric mixture of alginate and pullulan (Alg-Pll), in order to obtain materials that are suitable for subsequent implantation *in vivo*. Therefore, the scaffold thus obtained was subjected to cell viability and proliferation assays on two specific cultures to the proposed objectives.

Viability in fibroblast culture testing (Fig. 5.1.4.1 **a**) has been shown to be diminished, with a continuing decreasing from 24 to 48 hours. These results have put into difficulty the prospect of their use in future *in vivo* tests, and such cell proliferation is not compatible with the proposed objectives.

Also in the case of osteoblastic culture (Fig. 5.1.4.1 **b**), the results were comparable to those presented above, the composite samples having a high toxicity.

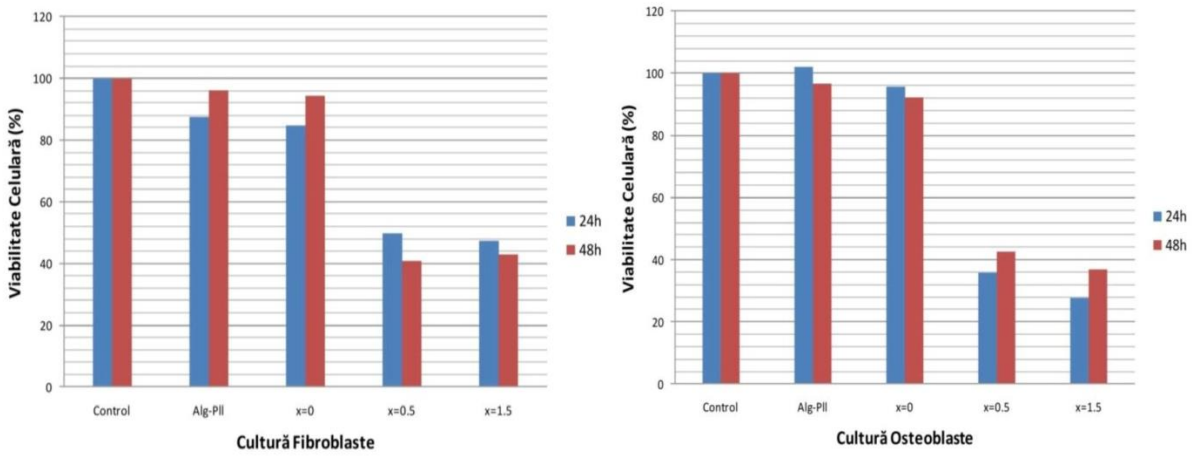

Fig. 5.1.4.1 Diagram of cell proliferation of Alg-PII-AgBG samples on a fibroblast (a) and osteoblast (b) culture.

5.2 Conclusions

In this study, based on the SiO_2-CaO-P_2O_5 primary formula, a wide palette of variable silver oxide compositions was synthesized. FT-IR and UV-Vis diffractograms and spectra showed structural characteristics indicating the bioactivity of all investigated samples. However, concentrations of 0.5 and 1.5 mol% of Ag2O have been found to be most suitable due to lack of AgCl formation and bioactive character.

6. SYNTHESIS AND CHARACTERIZATION OF SILICATE GLASSES DOPED WITH DIFFERENT CONCENTRATIONS OF GOLD NANOPARTICLES FOR THEIR APPLICATION IN TISSUE ENGINEERING

6.1 Results and discussions

6.1.1 Structural characterization

Free AuNP reveals a narrow plasmon band, in the visible spectrum, around 518 nm, characteristic AuP, spherical (Figure 6.1.1.1 **a**). After pluronic stabilization, a 2nm displacement of the absorption maximum (Figure 6.1.1.1 **a - red band**) can be observed, which can be attributed to the change of refractive index in the immediate vicinity of AuNP as a consequence of polymer adsorption.

These AuNPs were introduced into a silica glass matrix. In order to obtain more detailed information regarding the alternation of the size and morphology of nanoparticles, UV-vis absorption spectra were recorded during preparation and thermal stabilization (Fig. 6.1.1.1 **b**). Considerable shift of the red band (from 520 to 536 nm) (Figure 6.1.1.1 **a**) indicates the presence of larger nanoparticles. This behavior can be attributed to NP aggregation / agglomeration after inclusion in the glass matrix.

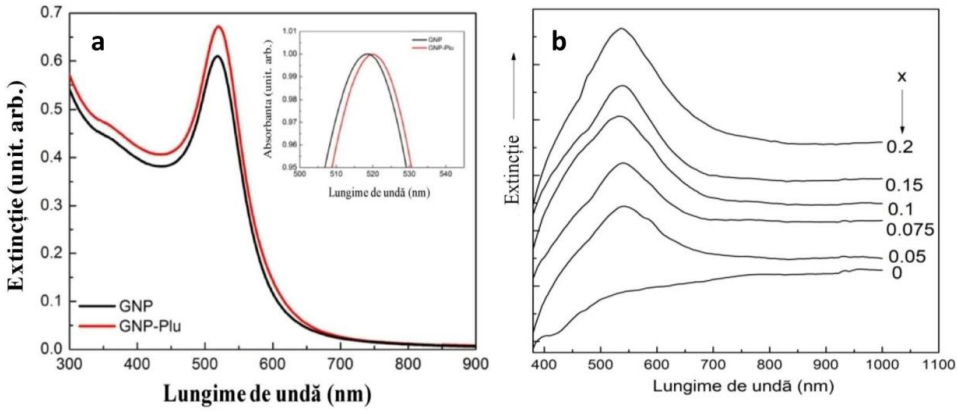

Fig. 6.1.1.1 Absorption spectra of synthesized AuNP (black line), AuNP stabilized with pluronic F127 (red line) in aqueous solution **(a)** and UV-vis spectra of glass samples in the system $60SiO_2 \cdot (32-x)CaO \cdot 8P_2O_5 \cdot xAu_2O$(mol%) **(b)**.

The diffractogram of the AuNP-free sample has, in particular, amorphous features, with some crystallinity outbreaks at $2\theta \sim 32$ °, which may be associated with the formation of the apatitic phase [82]. The presence of AuNP in the glass matrix was confirmed by the XRD patterns, where the diffraction lines can be associated with the planes (111), (200), (220) and (311) of a face from the cubic structure of Au (Fig. 6.1.1.2 **a**) [83].

FT-IR spectra of glass samples exhibit characteristic absorption bands specific to a silicate matrix, and as expected, spectral characteristics are not influenced by AuNP due to their low content (Fig. 6.1.1.2 **b**). Specific vibrational modes specific to Si-O-Si groups could be identified as follows: stretching modes Si-O-Si on 1080 and 1200 cm^{-1} [84,85], non-bonded Si-O-NOB silicon-oxygen stretches around the values 890-975 cm^{-1} [86], bending vibrations Si-O-Si la 800 cm^{-1} [84] și Si-O-Si la ~460 cm^{-1} [86]. The stretching vibrations of the phosphate groups occur in doublets at 565 and 604 cm^{-1} [84,87].

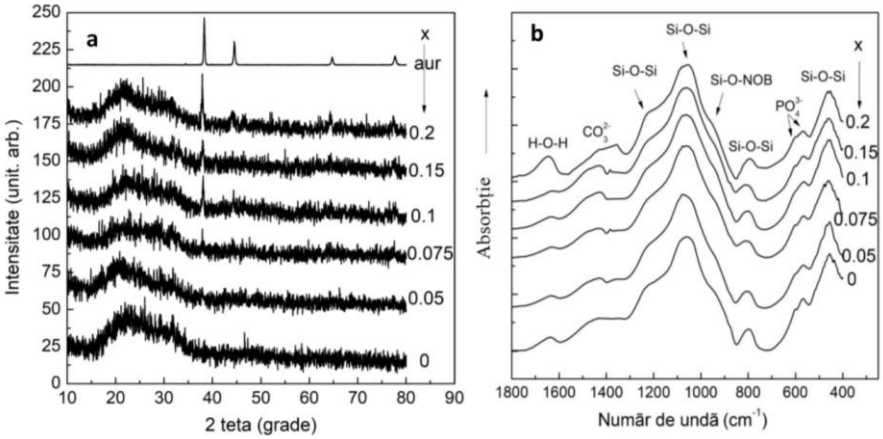

Fig. 6.1.1.2 Diffractograms (a) and FT-IR spectra (b) of the $60SiO_2 \cdot (32\text{-}x)\ CaO \cdot 8P_2O_5 \cdot xAu_2O$ (mol%) system samples. Gold diffractogram was included for comparative purposes.

6.1.2 Bioactivity

After 7 days of contact with SBF, the presence of self-assembled HAs can be observed. Thus, the presence of the crystalline HA phase is clearly visible in the diffractograms, as evidenced by all the samples, by the reflections recorded at 2θ=25,4° (002) and 2θ=31,5° (211) (Fig. 6.1.2.1 **a**). Broad diffraction signals between the 2θ = 30 ° and the 2θ = 34 ° angles correspond to the overlapping of the reflection planes (112), (300) and (202) of the crystalline HA [88]. Overlapping components begin to differentiate from the sample with x = 0.2. In the case of FT-IR spectra recorded after sampling in the SBF, the presence of the doublet located around the 604 and 564 cm^{-1} values becomes much more pronounced (Fig 6.1.2.1 **b**). These two bands are attributed to the bending vibrations of P-O and are characteristic signals of the crystalline HA phase [80,84].

The freshly formed HA is visible on the surface of all samples (Fig. 6.1.2.2). Although an apatite layer covers all samples, the SEM images show differences in the morphology of the formed layer, depending on the Au content, indicating the influence of AuNP on the bioactivity of the materials. As can be seen from Fig. 6.1.2.2, the presence of AuNP is beneficial in terms of the bioactivity of the samples. In the case of glass with x = 0.2 mol% Au2O, besides the spherical shape, three-dimensional flower-shaped nanostructures (Fig. 6.1.2.2).

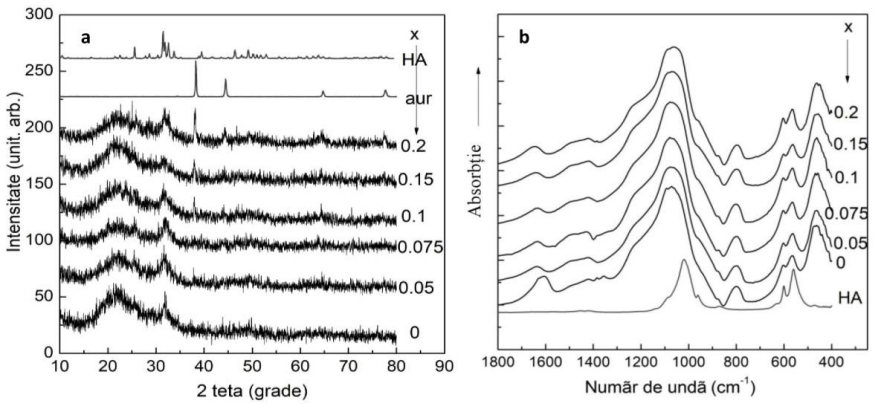

Fig. 6.1.2.1 Diffractograms (a) and FT-IR spectra (b) of samples from the $60SiO_2 \cdot (32\text{-}x)\ CaO \cdot 8P_2O_5 \cdot xAu_2O$ (mol%) system after immersion in SBF for 7 days. XRD diffractograms of gold and HA were included for comparative purposes.

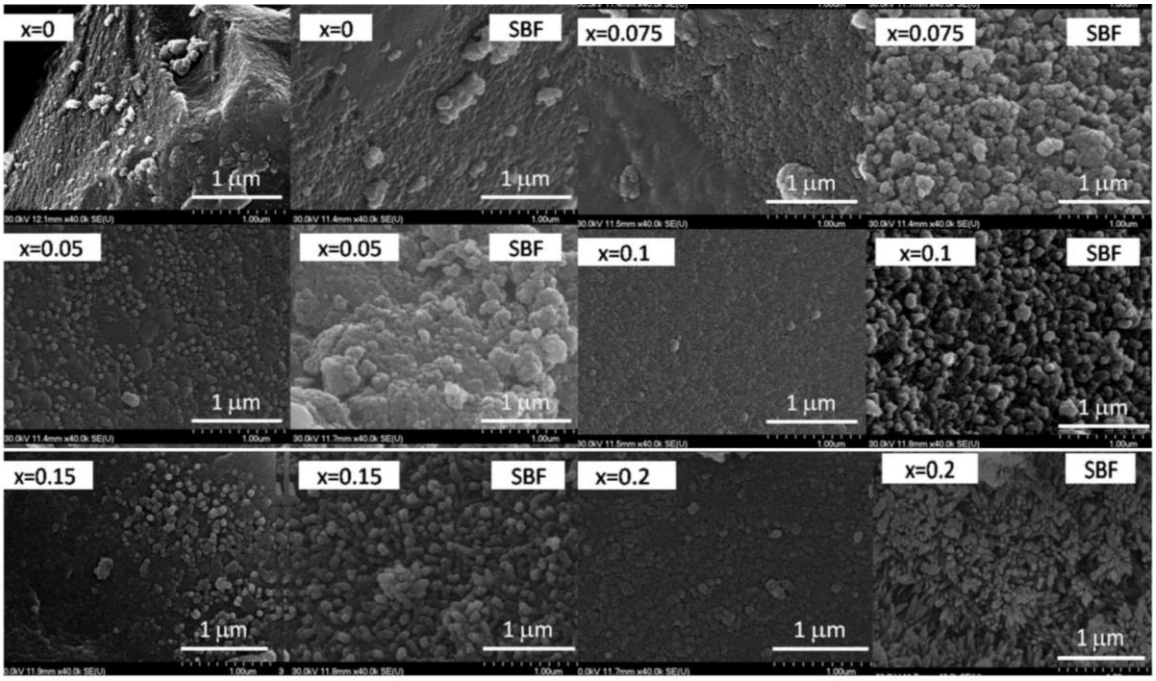

Fig. 6.1.2.2 SEM images from the $60SiO_2 \cdot (32\text{-}x)\ CaO \cdot 8P_2O_5 \cdot xAu_2O$ (mol%) system before and after immersion in SBF for 7 days.

6.1.3 Biocompatibility

FT-IR spectroscopy confirms the adsorption of BSA on the surface of the materials by the appearance of the absorption bands characteristic of the proteins: amide I (CO stretch modulus) at 1650 cm^{-1}, amide II (bending mode NH) at 1550 cm^{-1} and amide III (CN stretching and NH bending) around 1400 cm^{-1} (Fig. 6.1.3.1) [89].

Therefore, when the protein is attached to the surface, conformational changes occur, and usually the β-sheets release their structure, making them more flexible [90]. Exact această situație apare după adsorbția de BSA, structura sa secundară se modifică ușor prin scăderea valorii β-sheet-ului. Exactly this situation occurs after adsorption of BSA, its secondary structure changes slightly by subtracting the value of the β-sheet. At the same time, the α-helix

structure remains unchanged due to the fact that the three-dimensional structure of the protein is largely influenced and stabilized by the disulfide bridges of cysteine [91], that bind to AuNP. These results suggest that AuNP samples retain their biocompatibility.

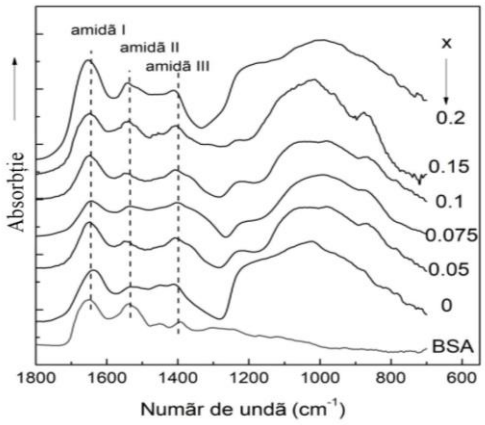

Fig. 6.1.3.1 FT-IR spectra of samples from the $60SiO_2$ system (32-x) $CaO \cdot 8P_2O_5 \cdot xAu_2O$ (mol%) after adsorption of BSA.

6.1.4 Cell viability

Last but not least, the in vitro cell viability test was also considered. Proliferation of human keratinocyte cells in the presence of glass samples was nearly or even greater than 100%, indicating good *in vitro* tolerance (Fig. 6.1.4.1). Therefore, the cytotoxic effect is minimal or even absent after an exposure period of 24 hours at 37°C. Starting with a glass concentration of 150 μg / ml, the HaCaT cell proliferation was promoted in particular by x = 0,15 și 0,2 Au_2O. Aceste valori au fost comparabile cu cele măsurate pe soluție coloidală de AuNP. The results obtained by us on the colloidal solution of AuNP are consistent with the previous reports of Lu et al. [92], where it was demonstrated that a low concentration of AuNP (16-51 nm) can stimulate the proliferation of keratinocyte cells. Therefore, these properties are maintained when the glass matrix contains at least 0,15 mol% Au_2O.

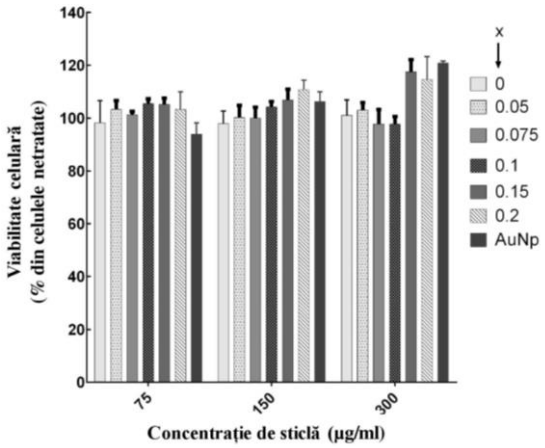

Fig. 6.1.4.1 The viability of keratinocyte cells after 24 hours of interaction with different glass concentrations in the $60SiO_2$ (32-x) $CaO \cdot 8P_2O_5$ system $\cdot Au_2O$ (mol%). The blank used was the colloidal solution of AuNP.

6.2 Conclusions

The sol-gel method has been successfully used to produce bioactive glasses doped with AuNP. Stabilization of the material was carried out at a temperature of 600°C. Diffractograms indicate both the amorphous structure of the glass matrix and the presence of AuNP. After the introduction of the samples into the SBF, the surface of them was identified with the presence of a self-assembled HA layer.

The amount of adsorbed BSA increased with the increase in the concentration of AuNP in the glass matrix. This process can be explained by the binding of cysteine to AuNP through strong Au-S interactions. Thanks to these linkages, the secondary BSA structure after adsorption changed slightly by subtracting the β-sheet value, confirming the good biocompatibility of the samples.

Cell viability after 24 hours of interaction with the studied materials showed very close or even greater than 100% values, highlighting good in vitro tolerance. In any case, human keratinocyte proliferation indices obtained on 0.15 and 0.20 mol% Au2O samples are very close to the values obtained on free AuNP, thus demonstrating the preservation of the properties of these nanostructures.

7. SYNTHESIS AND CHARACTERIZATION OF SILICATE GLASSES DOPED WITH COPPER OXIDE IN ORDER TO APPLY THEM IN BONE TISSUE ENGINEERING

7.1 Results and discussions

7.1.1 Structural characterization

The X-ray diffractograms obtained on the $60SiO_2$ (32-x) $CaO \cdot 8P_2O_5 \cdot xCuO$ (mol%) system samples are predominantly amorphous (Figure 7.1.1.1-**a**). The irregular shape of the signals may be caused by the presence of the second signal that occurs around $2\theta \sim 32°$, indicating the existence of several crystallization outbreaks associated with the formation of the apatitic phase [77,93–96]. This signal has the highest intensity on the samples with a copper oxide content ≤ 1.5 mol%. In the case of 4 mol% CuO, this signal can not be clearly distinguished, but instead, at this concentration, the crystal signature of the calcium carbonate (the highest value $2\theta = 29.8$ °) can be observed. This change may seem undesirable but has been previously reported [97], with no adverse effects on the bioactivity of the samples, because it is a precursor of the carbonate apatite layer formed in the SBF [77,97].

FT-IR spectra have absorption bands characteristic of silicate bioactive and glass-ceramics (Figure 7.1.1.1-**b**). Thus, characteristics attributable to Si-O-Si (1040 and 860 cm^{-1}) vibration stresses and Si-O-Si bending vibrations (465 cm^{-1}) [77]. The maximum intensity of the vibrational stretching signal of the Si-O-Si group showed a slight increase with the addition of copper oxide. The band appearing at 1440 cm-1 can be associated with the existence of carbonate groups [77], while twin signals of 560 and 580 cm^{-1} are attributed to phosphate groups [77]. In samples with 2.5 and 4 mol% CuO, changes in the shape of the doublet around 600 cm^{-1} can be distinguished, and this becomes wider, with the appearance of another absorption signal. One possible explanation may be the overlapping of the phosphatic groups with the vibrational signal of CuO. The copper oxide IR signals of 603 and 497 cm^{-1} are known due to the stretching modes of Cu-O along the direction [101] [98]. Moreover, other IR-active modes for Cu-O have been reported in a spectral range between 605 and 660 cm^{-1}, which may be associated with the existence of another Cu_2O phase [98]. It is also worth mentioning the absorption bands of 1400 to 1500 cm^{-1} given by the vibrations of the carbonate groups.

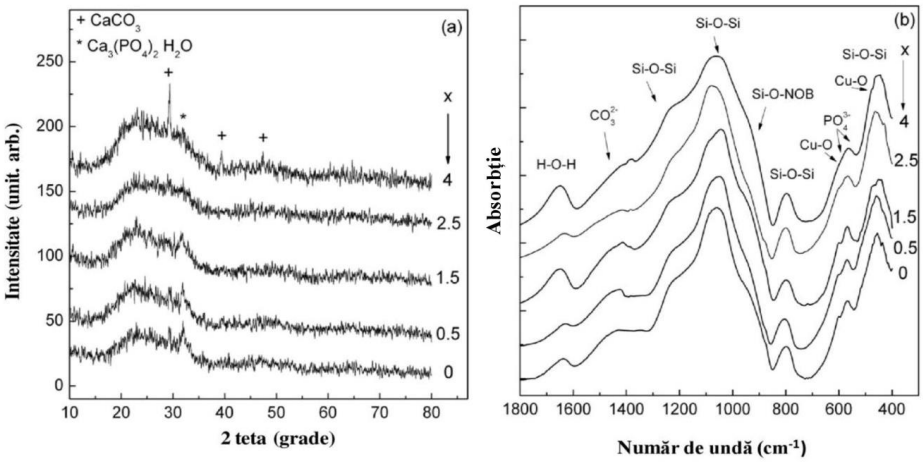

Fig. 7.1.1.1 Diffractograms XRD **(a)** and FT-IR spectra of samples in the system $60SiO_2 \cdot (32\text{-}x)CaO \cdot 8P_2O_5 \cdot xCuO$(mol%) **(b)**.

In Figure 7.1.1.2, you can see TEM images purchased from the samples with 0.5 mol% CuO. Black points are crystalline structures, and HRTEM images were recorded to determine their nature (Figure 7.1.1.2 **b**). The image of the Fourier transform (Figure 7.1.1.2 **c**), based on Fig. 7.2.1.2 **b**, expose the measurements of the interplanar spacings of 0.311 and 0.202 nm, values that are consistent with those obtained with the calcium carbonate planes (104) and (018) [99].

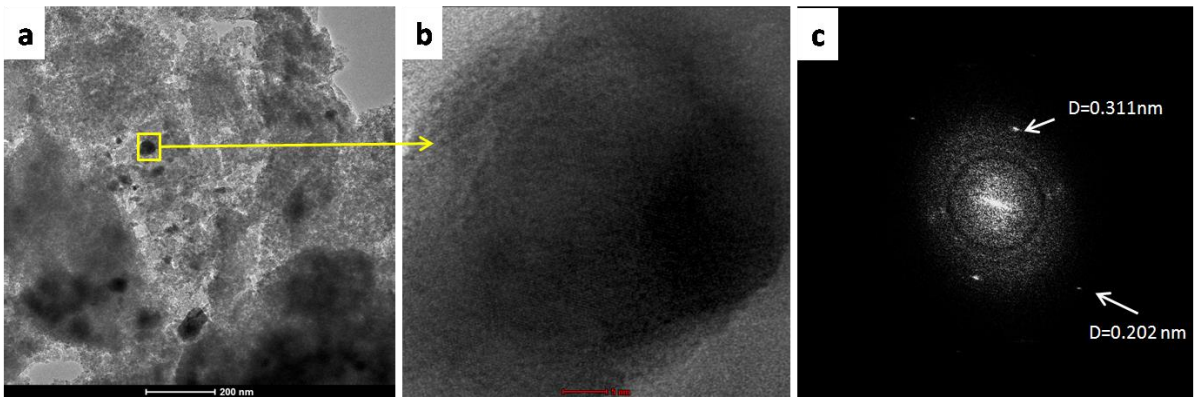

Fig. 7.1.1.2 TEM (a - 200 nm scale), HRTEM (b - 5 nm scale) and DFE on HRTEM (c) images of the system samples $60SiO_2 \cdot (32\text{-}x)CaO \cdot 8P_2O_5 \cdot xCuO$(mol%), x=0,5.

Furthermore, in order to achieve a more in-depth characterization, Uv-vis absorption measurements were used. Looking at the spectra of Fig. 7.1.1.3, it can be noticed that the copper oxide containing samples have a dominant broad band, centered around 800 nm, characteristic of the octahedral coordination of d-d transition of Cu^{2+} [100]. As expected, this signal increases in intensity as the amount of added CuO increases. The width of the absorption band can be attributed to the overlapping of metallic copper and Cu-ion signals, the latter giving rise to large electronic absorption signals at a value greater than 700 nm [101,102].

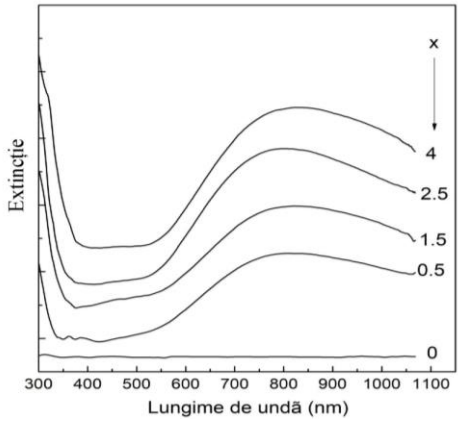

Fig. 7.1.1.3 The UV-vis spectra of the samples in the system $60SiO_2 \cdot (32\text{-}x)CaO \cdot 8P_2O_5 \cdot xCuO$(mol%).

The data obtained from the BET analyzes showed a progressive increase in the area and the average pore volume distribution, starting with the undoped matrix and up to 1.5 and 2.5 mol% CuO samples. Figure 7.1.1.4 (a) reveals the largest specific area at the sample with 1.5 mol% CuO, and Figure 7.1.1.4 (b) indicates the highest average pore volume in the sample with 2.5 mol% CuO.

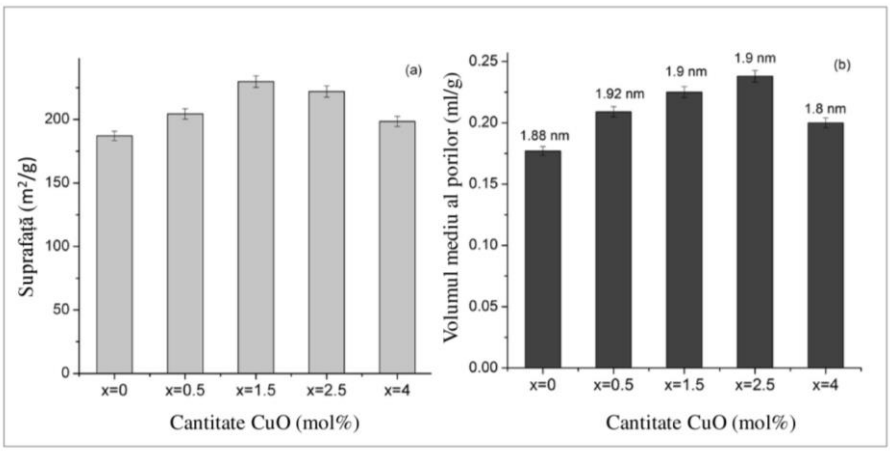

Fig. 7.1.1.4 BET surface (a) and volume distribution of pores (b) of samples in the system $60SiO_2 \cdot (32\text{-}x)CaO \cdot 8P_2O_5 \cdot xCuO$(mol%).

7.1.2 Bioactivity

After a period of 7 days in SBF, the apatitic phase is recorded in diffractograms by the signals from $2\theta \sim 26$ ° and 32 °, these being superimposed with the apatitic phase already existing in the samples (Figure 7.1.2.1 **a**). To facilitate comparison, in Fig. 7.1.2.1 the HA diffractogram was introduced [80].

In the FT-IR spectra of the samples introduced in the SBF (Figure 7.1.2.1 **b**), the crystalline HA-specific bands at the values of 604 and 564 cm^{-1} increase in intensity from those measured on the untreated samples. Moreover, the 4 mol% CuO glass (Figure 7.1.2.1 **b**)

expresses a well-defined double crystalline HA (604 and 564 cm^{-1}). These bands do not appear as two distinct absorption signals in sample spectra before immersion in the SBF.

Figure 7.1.2.2 **a-e** presents SEM images of structures in the $60SiO_2$ system (32 - x) CaO · $8P_2O_5$ · xCuO (mol%) prior to introduction into SBF and confirms the existence of surface crystalline morphology, which strengthens the findings derived from the analyzes XRD and FT-IR.

Apatitic layer formation on the surface of ceramic bottles after their immersion in SBF was also observed by scanning electron microscopy. Figure 7.1.2.2 **f-j** shows the surface morphology of glass specimens incubated for 7 days in SBF. Almost every sample surface (Fig 7.1.2.2 **f-h, j**) indicates bundles with cauliflower morphology covering the entire area, except for the material with 2.5 mol% of CuO, which reveals the formation of submicrometric apatite grains.

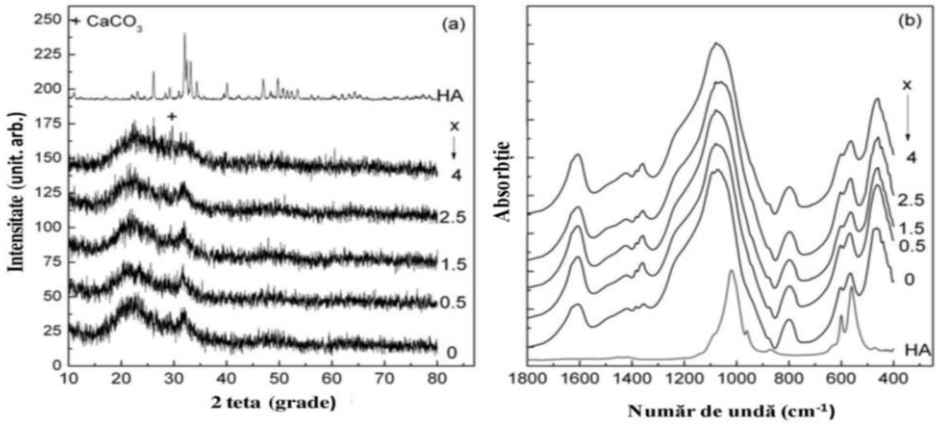

Fig. 7.1.2.1 Diffractograms (a) and FT-IR (b) spectra of the 60SiO2 · (32-x) CaO · 8P2O5 · xCuO (mol%) system after insertion in the SBF for 7 days. The diffractogram and FT-IR spectrum of HA were introduced for comparative purposes only.

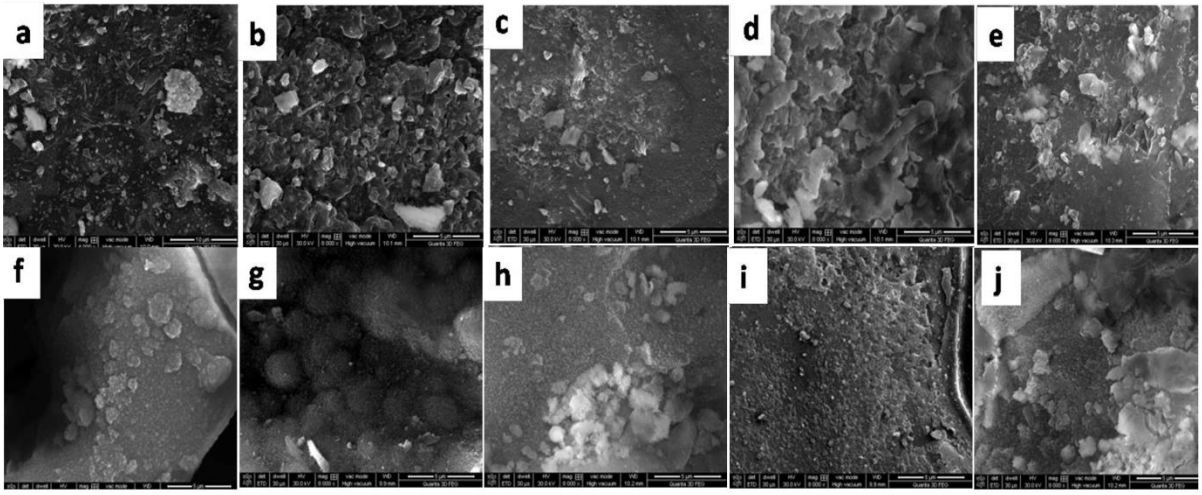

Fig. 7.1.2.2 SEM images in the $60SiO_2$ system; (32-x) CaO · $8P_2O_5$ · xCuO (mol%) before (a) x = 0; (b) x = 0.5; (c) x = 1.5; (d) x = 2.5; (e) x = 4 (a-e) and after immersion in SBF for 7 days (f) x = 0; (g) x = 0.5; (h) x = 1.5; (i) x = 2.5; (j) x = 4, at a 5 μm scale.

7.1.3 Ion release

Copper ions have proven to be important components both in angiogenesis processes and in microorganism control mechanisms [103]. To analyze the amount of Cu released from our samples in 24 hours, measurements were made by inductively coupled plasma mass spectrometry (ICP-Q-MS) (Figure 7.1.3.1 **a**). Quantification of the total amount of copper was achieved by dissolving the samples in a mixture of acids (Figure 7.1.3.1 **b**). The obtained results show that ion release is dependent on the Cu concentration of the samples, the higher the amount released is higher. Thus, it can be seen that at a sample concentration of 0.5 mol% CuO, the release is 0.135 mg / L and at a concentration of 4 mol% CuO material, the release reaches a value of 8.429 mg / L (Fig. 7.1.3.1 **a**).

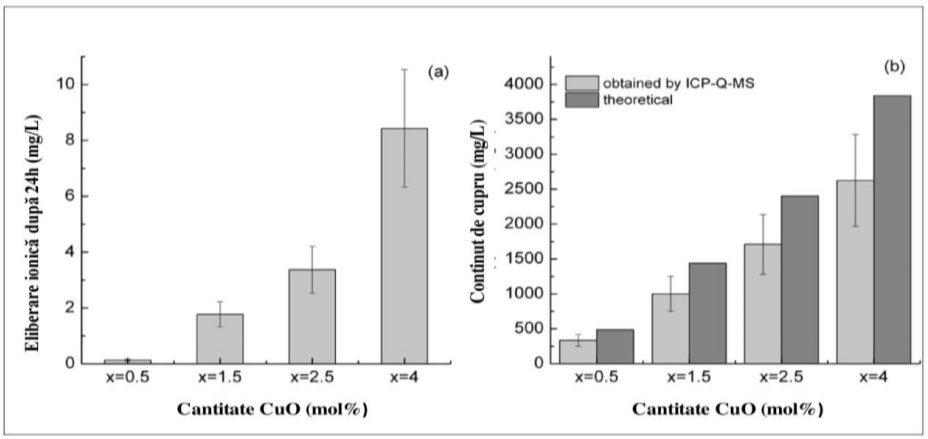

Fig. 7.1.3.1 The copper ion release from the samples of the $60SiO_2$ system (32-x) $CaO \cdot 8P_2O_5 \cdot xCuO$ (mol%) immersed for 24h in deionized water **(a)** and the total copper content of the samples dissolved in a mixture of acids **(b)**.

7.1.4 Antibacterial activity

The antibacterial activity of the ceramic samples studied was tested on two bacterial reference cultures for in-hospital infections. CMI and CMB were used as standard qualitative methods for determining the antimicrobial reactivity of the tested materials. CMI represents the smallest concentration of substance that can stop bacterial growth after an incubation period of 24 hours [104], whereas CMB represents the lowest concentration of substance used to kill a bacterial population [104]. The inhibitory effect of the studied materials was more significant on the *Pseudomonas aeruginosa* strain than on the *Staphylococcus aureus* strain. The lowest amount of copper oxide was also most effective in both bacterial cultures (Figure 7.1.4.1 **a**). The sample with 0.5 mol% of CuO also showed a very good bactericidal activity, for the other concentrations a larger amount of sample was required to combat bacteria (Fig. 7.1.4.1 **b**).

The presence of isolated copper species in the sample with 0.5 mol% of CuO may lead to an increase in antimicrobial efficacy. In fact, samples with a higher concentration of copper oxide release the Cu species more easily, but their antibacterial efficacy is lower compared to the sample with 0.5 mol% of CuO, most likely because of larger sizes.

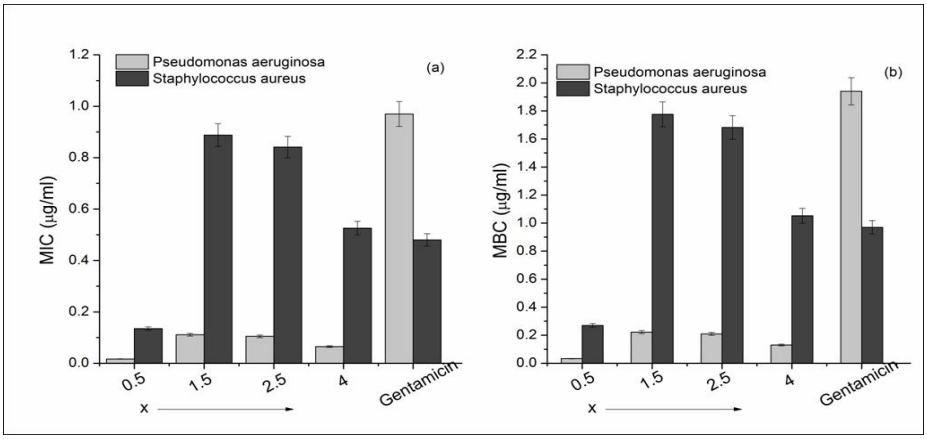

Fig. 7.1.4.1 Minimum inhibitory concentration (MIC) **(a)** and minimal bactericidal concentration (CMB) **(b)**.

7.1.5 Biocompatibility

Further, the samples were subjected to protein adsorption assays for biocompatibility testing. The results obtained after adsorption of BSA on the surface of the bottles showed characteristic protein bands: amides I (CO stretching) at 1650 cm-1 and amides II (bending NH) at 1550 cm-1 (Figure 7.1.5.1) indicating the presence of proteins on the surface of the materials [89]. It is well known that the protein configuration changes with their adsorption on the sample surface due to the electrostatic and hydrogen bonds created [105,106].

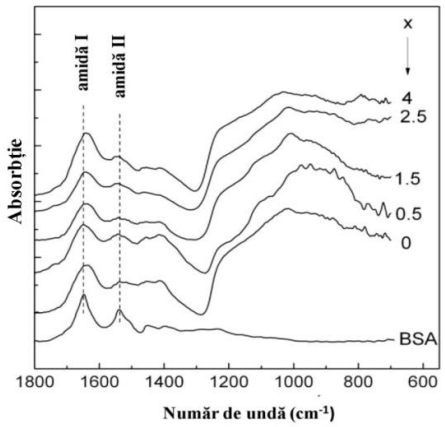

Fig. 7.1.5.1 FT-IR spectra of the $60SiO_2$ (32-x) CaO · $8P_2O_5$ · xCuO (mol%) samples after protein adsorption.

7.1.6 Cell viability

The results show that the cytotoxic effect is almost absent after a 24h exposure for both dilutions (Fig. 7.1.6.1).

In this study, the HaCaT cell proliferation was significantly promoted by samples containing 0.5 and 1.5 mol% CuO, compared to copper-free bottles. Viability for the other two samples (x = 2.5 and 4) approaches 100%, suggesting good *in vivo* tolerance.

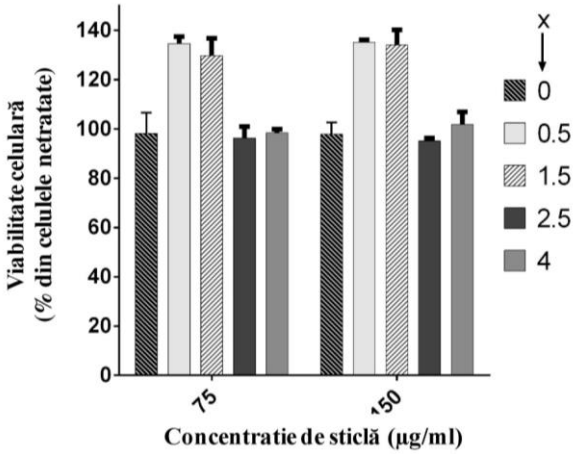

Fig. 7.1.6.1 Testing cell viability of samples in the system $60SiO_2 \cdot (32\text{-}x)CaO \cdot 8P_2O_5 \cdot xCuO$(mol%).

7.2 Conclusions

The sol-gel synthesis method has been successfully used to obtain ceramic bottles (SiO2-CaO-P2O5) with different concentrations of copper oxide (x = 0.5, 1.5, 2.5 and 4 mol% CuO) to determine the properties required to include these materials in tissue engineering applications. UV-vis spectra and TEM analyzes showed that all samples contained both ionic and metallic copper species. BET tests have shown that the 1.5 mol% CuO sample has the largest specific surface area and the silica matrix with 2.5 mol% CuO has the highest pore volume.

Information derived from the XRD, FT-IR and SEM measurements performed on samples immersed in SBF has demonstrated the existence of HA crystals, a result that confirms the *in vitro* bioactivity of all studied materials.

It was found that the minimal inhibitory effect of the studied samples was more pronounced on the *Pseudomonas aeruginosa* strain than that of *Staphylococcus aureus*, although the sample with the concentration of 0.5 mol% of CuO was effective in combating both bacterial cultures. Also, the sample with the lowest CuO content showed the best bactericidal activity. BSA adsorption on the sample surface showed that binding of Cu species caused minor changes in protein conformation, the final conclusion being that all samples are biocompatible. As regards the cytotoxicity of the materials, this is close to 0% after a standard exposure of 24 hours in both dilutions. Samples of 0.5 and 1.5 mol% of CuO have shown a very high cell proliferation rate.

Based on the fact that the investigated ceramic bottles showed good bioactivity and biocompatibility, samples with 0.5 and 1.5 mol% CuO showed excellent viability and the material with 0.5 mol% CuO had good results in the control of the strain of *Staphylococcus aureus*, we can conclude that the matrix containing 0.5 mol% of CuO is the most suitable for future in vivo tests.

8. SYNTHESIS, CHARACTERIZATION, *IN VITRO* TESTING AND *IN VIVO* IMPLANTATION OF A BIOACTIVE GLASS-POLYMER BASED COMPOSITE FOR EXPERIMENTAL AND COMPARATIVE PURPOSES

8.1 Results and discussions

8.1.1 Structural characterization

Diffractograms of glass samples in the xCuBG system (x = 0, 0.5 and 1.5 mol%) prepared by the sol-gel method have an amorphous structure with the appearance of several crystallization centers associated with the formation of the apatitic phase (Fig. 8.1.1.1 **a**) [93]. FT-IR spectra of bioactive ceramic materials (Figure 8.1.1.1 **b**) indicate typical characteristics for silicone networks (Si-O-Si vibrations at 1040 and 860 cm^{-1} and vibration Si-O-Si at 465 cm^{-1}) [84]. The bands around the values of 604 and 565 cm^{-1} are attributed to the vibration of the phosphate groups [84]. The stretch signals of the Cu-O group occur at 603 and 497 cm^{-1} and overlap with strips from the phosphate groups [98,107].

The composite structures Alg-Pll-xCuBG (x = 0, 0.5 and 1.5 mol%) are amorphous, as can be seen from the XRD diffractograms (Fig 8.1.1.1 **a**), and FT-IR spectra show vibrations predominant to the polymer units (Fig 8.1.1.1 **b**). Thus, pullulan bands at 1636, 1354 and 1080 cm^{-1} are attributed to the tensile and bending vibrations of O-C-O, C-O-H and C6-OH respectively [108]. The bands corresponding to sodium alginate of 1600 and 1400 cm^{-1} can be attributed to the asymmetric stretching vibrations of the COO- group. Signals located at 1158 and 1116 cm^{-1} may be associated with the C-O stretching vibrations, while at 1560 cm^{-1} the C = C stretching vibration [109]. Thus, they are C = C and O-C-O, belonging to the structure of Si-O, Si-O-NOB or Si-O-Si polymers and SiO4 tetrahedral units. Therefore, the interaction between the polymer mixture (Alg-Pll) and the bioactive glass was evidenced by the displacement of the C6-OH band from 1080 to 1090 cm^{-1} and the increase in the intensity of the 1636/1560 cm^{-1} ratio representing the stretching vibrations of OCO and C = C groups (Fig. 8.2.1.1 **b**).

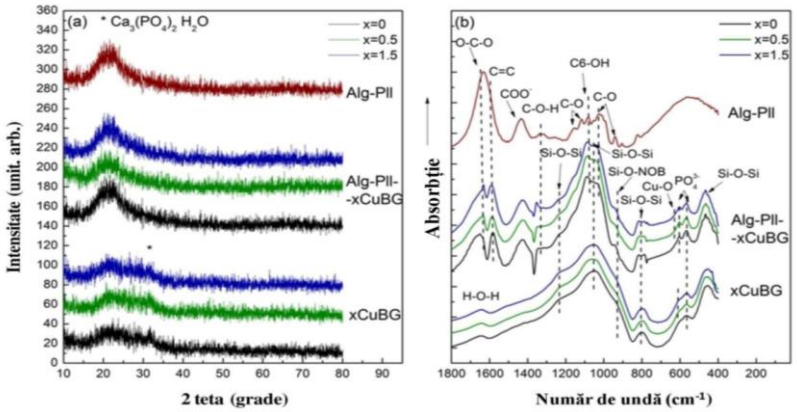

Fig. 8.1.1.1 XRD diffractograms **(a)** and FT-IR **(b)** spectra of ceramic glasses xCuBG (x = 0, 0.5 and 1.5 mol%) and Alg-PII-xCuBG composite samples (x = 1.5 mol% CuO).

8.1.2 Cell viability

Since the final destination of these materials involves implantation in vivo, the next step in this regard was the in vitro cytotoxicity test for these composites. Thus, the use of Alamar-Blue kit showed greater sensitivity of osteoblast culture compared to that of fibroblasts. However, proliferation rates were between 75 and 96% for fibroblasts (Figure 8.1.2.1 **a**) and 55 to 101% for osteoblasts (Figure 8.1.2.1 **b**). An increase in viability from 24 to 48 hours can be observed in almost all the investigated samples. The results indicate good long-term cell proliferation and minimal cytotoxicity, further testing these composite materials in in vivo experimental studies.

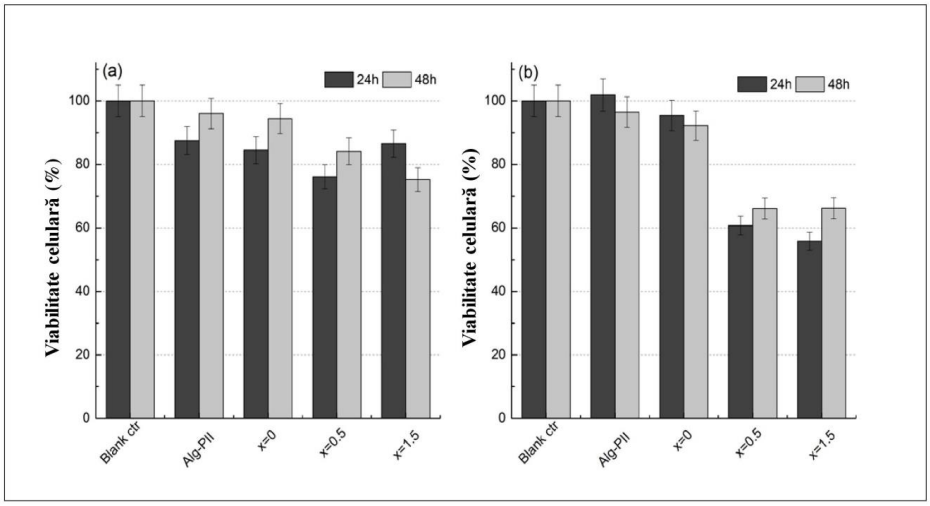

Fig. 8.1.2.1 Viability of fibroblast cells **(a)** and osteoblasts **(b)** after 24 and 48 h on Composite samples Alg-Pll and Alg-Pll-xCu · BG (x = 0, 0.5 and 1.5 mol% CuO). Neutralized cell cultures were used as controls.

8.1.3 *In vitro - in vivo* biocompatibility

As a result of in vitro bioactivity testing, scaffolds were introduced into the SBF. In parallel, they were implanted subcutaneously and intramuscularly in the rat (Fig. 8.1.3.1).

Materials have been successfully accepted by target tissues, showing no inflammation, infection or rejection signs, thus proving good biocompatibility *in vivo*.

Fig. 8.1.3.1 Digital photos taken at necropsy (one can see the attachment of composite material to subcutaneous connective tissue).

From the diffractograms the signature of the crystalline apaticitic phase (Fig.8.1.3.2 **a**) is highlighted by the signal located at 20 = 32.28 °, which corresponds to the reflection plane (112) of the crystalline hexagonal structure HA [80]. The XRD diffractograms recorded on postimplant samples (Figure 8.1.3.2 **b**) indicate the presence of an additional signal at 2θ = 25.9 ° corresponding to the reflection plane (002) of HA structure [80].

The FT-IR spectra (Figure 8.1.3.2 **a1**) confirm the above results. Samples taken from the SBF mark the strips characteristic of the P-O groups at 602 and 560 cm^{-1} and PO_4^{3-} at 1040 cm^{-1}, these being associated with the formation of the calcium phosphate layer [86]. Post *in vivo*, the vibration signals of the P-O group at 602 and 560 cm^{-1} become more prominent compared to the corresponding bands recorded after the in vitro tests. The signal from the PO_4^{3-} (1040 cm^{-1}) group becomes sharper, also suggesting the formation of the calcium phosphate layer (Fig 8.1.3.2 **b1**).

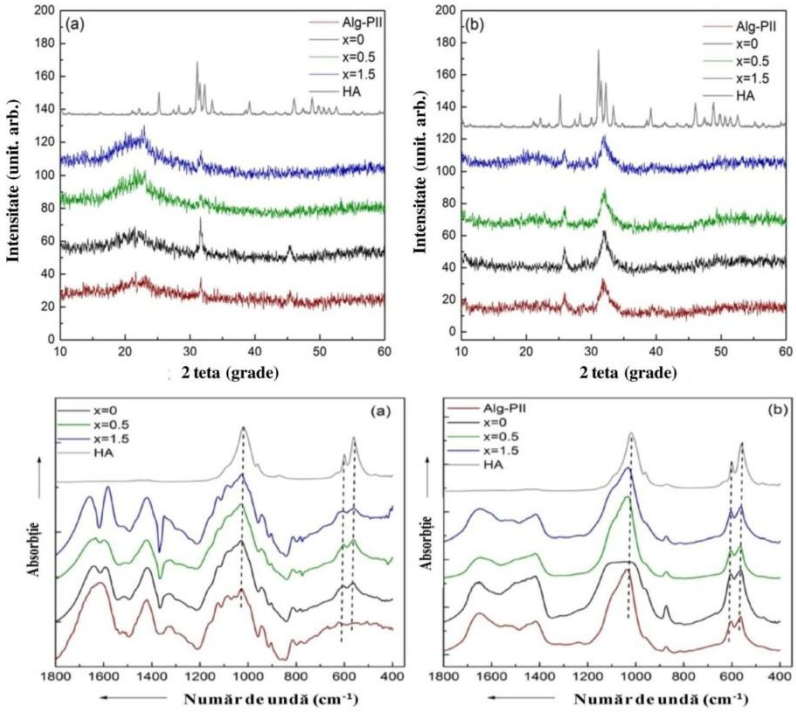

Fig. 8.1.3.2 Diffractograms of Alg-Pll-xCu · BG and FT-IR spectra after immersion in SBF **(a and a1)** and post *in vivo* **(b and b1).**

In Fig. 8.1.3.3 **col. 2**, the formation of the HA layer on the surface of the material can be observed. It has the appearance of a microstructure composed of beads. The *in vivo* images (Figure 8.1.3.3 **column 3**) reveal agglomerated beads with a size of approximately 75-100 nm.

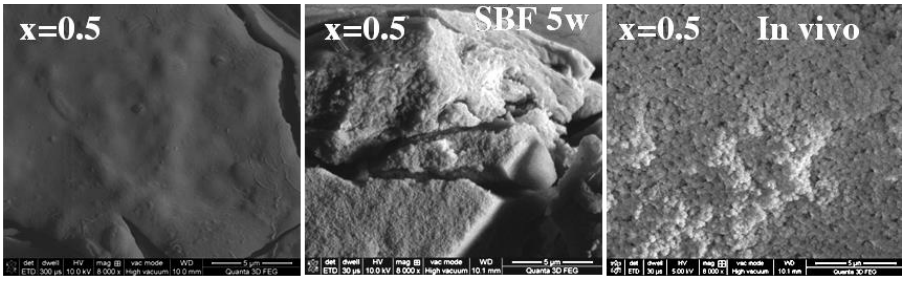

Fig. 8.1.3.3 SEM images of Alg-Pll-xCu · BG unchanged (**column 1**) after immersion in SBF (**column 2**) and post in vivo (**column 3**). Measuring scale: 5 μm.

8.1.4 *In Vivo* imaging evaluation

We opted for using the MRI exam as a bone imaging technique to track not only implant-induced changes in bone tissue but also changes that may occur in soft tissue adjacent to primary lesion and changes in bone marrow.

For each animal, a sagittal scan was performed using the FLASH protocol (gradient echo), the weighted sequence **T1**.

After 28 days postoperatively, in the first group **(A, E)**, the discontinuity of the bone compact is no longer present, being a continuous, circular, hyperdense, lesion demyelinating region, comprising both the compact bone and the medial region given the recovery of bone tissue and vascular regeneration, the surface of the bone is irregular with the presence of a periosteum. In group two **(B, F)** the bone surface is smooth with discreet periosteality, the area of demarcation is much lower compared to the first group (Fig 8.1.4.1).

The occurrence of hyposemnal in the weighted T1 sequence is characteristic for acute or chronic hemorrhage, edema or calcification. The hypersensitivity aspect of the intramedullary reaction correlated with the histopathological examination corresponds to the occurrence of hypervascularization at the implant area and the formation of bone tissue.

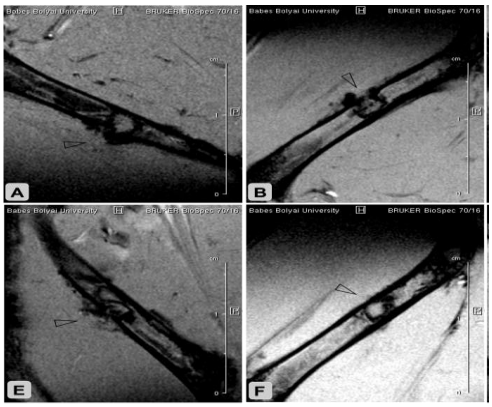

Fig. 8.1.4.1 Post-operative MRI images (the first line represents the right posterior limb of each group **A - Alg - Pll - 0,5CuBG; B - Alg - Pll - 1,5CuBG**) and the second line represents the left posterior member of each group **E, F - Alg -Pll-βTCP / HA**).

8.1.5 Histopathological evaluation

In the images shown in Fig. 8.1.5.1 **A-B** shows the longitudinal sections of the femur bone with asterisk marking the composite material implanted in each batch and the double arrow indicating the defect boundaries. It can be seen that the implanted scaffold was partially or completely surrounded by trabecular bone (Fig. 8.1.5.1 **A-B dotted border**).

Column A, belongs to the commercial material samples, in vivo, for comparative purposes. Figure **A1** closes in detail the marked area in Section **A**, identifying the bony spikes that completely surround the implanted structure.

Column B, describes the group implanted with Alg-PII-0.5CuBG. Figure **B1** details the dotted dotted area of **Image B**. Thus, the spongy bone that surrounds the surface of the scaffold is found.

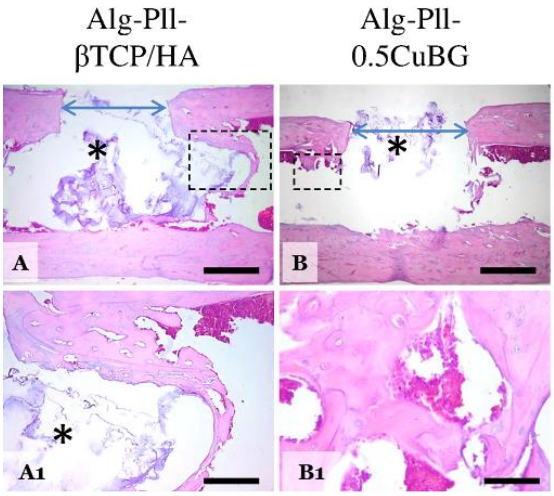

Fig. 8.1.5.1 Histological sections of composite scaffolds implanted in the femoral compact (**A-B**) and bone tissue interactions with the material **(A1 – B1)**.

8.3 Conclusions

Composite materials Alg-PII-xCuBG (x = 0, 0.5 and 1.5 mol% CuO) were synthesized, characterized and successfully investigated *in vitro* and *in vivo*. FT-IR spectra reveal the bonds between the two polymers and the bioactive glass. The polymers and glass bands exhibit displacements in the composite structure spectra. Viability tests indicate better long-term results for both cell cultures.

XRD and FT-IR analyzes showed significant differences in intensity between *in vitro* and *in vivo* results, on the one hand confirming the bioactive and biocompatible properties of the studied samples and on the other hand effective HA formation and solid fusion with tissue alive. SEM images confirmed the results of XRD and FT-IR analyzes. On samples extracted from in vivo, nano-aggregate beads and nanoparticles became more prominent.

Bone implantation proceeded according to the initial protocol, the implanted materials being well tolerated by the bone and neighboring tissues. MRI scans allowed non-invasive and non-destructive analysis of materials in vivo without affecting the final results. The histopathological examination confirmed that the groups implanted with the studied materials were the most effective in terms of healing and regeneration capacity, more active than the control group.

9. OVERALL CONCLUSIONS AND PERSPECTIVES

9.1 Overall conclusions

In the first study of this paper, the synthesis and characterization of silicate materials with addition of Ag_2O was successfully performed. The characterization methods used have proven the bioactivity of the studied bottles, and the viability obtained was good. However, their inclusion in a polymeric mixture led to the production of relatively high toxicity composites, which were incompatible with the originally proposed targets.

The second study of the thesis consisted in the synthesis and characterization of silicate glasses doped with AuNP and resulted in positive results. *In vitro* bioactivity was demonstrated by introducing samples into the SBF. Also the biocompatibility of the materials was highlighted by the amount of adsorbed BSA. Cell viability indicated values close to 100%, suggesting good *in vitro* tolerance. Bioactive materials have been obtained that have effectively embedded AuNP without the presence of other Au species, but with different sizes of NP.

In study number three of this paper, we have succeeded in optimizing silicate glasses with the addition of CuO. Thus, from the initial four concentration ranges, through the structural characterization and *in vitro* testing methods, the two most suitable concentrations were selected for future *in vivo* experimental studies. Amounts of 0.5 and 1.5 mol% of added CuO have proved to be most suitable for antibacterial activity and cell proliferation. Considering that all four ceramic glasses investigated showed good bioactivity and biocompatibility, the final selection was developed taking into account the results of the *in vitro* tests.

The latter study involved the inclusion of CuO-addition materials previously developed in a polymer blend and the development of an *in vivo* bone regeneration experiment. In this way, the two optimized compositions of bioactive glasses found in the previous study were furter used in order to obtain composite materials. The results obtained comparatively between the studied materials and the commercial product revealed the special qualities of the studied samples, result that demonstrates the repair capacity of the bone tissue, when the optimized compositions are used, their performances being at least as good as that of the standardized material.

9.2 Perspectives

The biomaterial branch, a field of wide interest among researchers around the world, tends to become an increasingly appreciated option and used in modern medicine. Thus, the topics discussed in this paper could be developed effectively in the years to come, through experimental studies on various animal species, in order to gain a sufficient experience of progress towards clinical trial on human patients.

LITERATURE

[1] J.F.A. Valente, T.A.M. Valente, P. Alves, P. Ferreira, A. Silva, I.J. Correia, Alginate based scaffolds for bone tissue engineering, Mater. Sci. Eng. C. 32 (2012) 2596–2603. doi:10.1016/j.msec.2012.08.001.
[2] M.J. Lysaght, A. Jaklenec, E. Deweerd, Great expectations: private sector activity in tissue engineering, regenerative medicine, and stem cell therapeutics, Tissue Eng. Part A. 14 (2008) 305–315.
[3] M.N. Rahaman, Bioactive ceramics and glasses for tissue engineering, in: Tissue Eng. Using Ceram. Polym., Elsevier, 2014: pp. 67–114. doi:10.1533/9780857097163.1.67.
[4] P. V Giannoudis, H. Dinopoulos, E. Tsiridis, Bone substitutes: an update, Injury. 36 (2005) S20–S27.
[5] J.R. Pleis, M. Lethbridge-Çejku, Summary health statistics for US adults: National Health Interview Survey, 2005., Vital Health Stat. 10. (2006) 1–153.
[6] D.W. Hutmacher, Scaffolds in tissue engineering bone and cartilage., Biomaterials. 21 (2000) 2529–2543. doi:10.1016/S0142-9612(00)00121-6.
[7] J.S. Walsh, Normal bone physiology, remodelling and its hormonal regulation, Surg. 33 (2015) 1–6. doi:10.1016/j.mpsur.2014.10.010.
[8] N. Little, B. Rogers, M. Flannery, Bone formation, remodelling and healing, Surg. 29 (2011) 141–145. doi:10.1016/j.mpsur.2011.01.002.
[9] T.J. Martin, K.W. Ng, G.C. Nicholson, Cell biology of bone, Baillieres. Clin. Endocrinol. Metab. 2 (1988) 1–29.
[10] J.J. PRITCHARD, General Histology of Bone, in: Biol. Physiol. Bone, Elsevier, 1972: pp. 1–20. doi:10.1016/B978-0-12-119201-3.50008-1.
[11] S. Weiner, H.D. Wagner, The material bone: structure-mechanical function relations, Annu. Rev. Mater. Sci. 28 (1998) 271–298.
[12] L.L. Hench, J. Wilson, An introduction to bioceramics, World scientific, 1993.
[13] L.L. Hench, Biomaterials: a forecast for the future, Biomaterials. 19 (1998) 1419–1423.
[14] L.L. Hench, J. Wilson, Clinical performance of skeletal prostheses, Springer, 1996.
[15] J. LeFanu, The Fall and Rise of Modern Medicine, Little Brown. (1999) 104–113.
[16] S. Simon, Orthopaedic basic scienceAmerican Academy of Orthopaedic Surgeons, Rosemont, IL. (1994).
[17] L.L. Hench, J.K. West, Biological applications of bioactive glasses, Harwood Academic Publishers, 1996.
[18] L.L. Hench, Bioceramics: From Concept to Clinic, J. Am. Ceram. Soc. 74 (1991) 1487–1510. doi:10.1111/j.1151-2916.1991.tb07132.x.
[19] L.L. Hench, J.R. Jones, P. Sepulveda, Bioactive Materials for Tissue Engineering Scaffolds, in: Futur. Strateg. Tissue Organ Replace., IMPERIAL COLLEGE PRESS, 2002: pp. 3–24. doi:10.1142/9781860949647_0001.
[20] J. Livage, C. Sanchez, Sol-gel chemistry, J. Non. Cryst. Solids. 145 (1992) 11–19.
[21] T. Coradin, M. Boissière, J. Livage, Sol-gel chemistry in medicinal science, Curr. Med. Chem. 13 (2006) 99–108.
[22] I.A. Aksay, S. Weiner, Biomaterials is this really a field of research?, Curr. Opin. Solid State Mater. Sci. 3 (1998) 219–220.
[23] H. Hajiali, S. Karbasi, M. Hosseinalipour, H.R. Rezaie, Preparation of a novel biodegradable nanocomposite scaffold based on poly (3-hydroxybutyrate)/bioglass nanoparticles for bone tissue engineering, J. Mater. Sci. Mater. Med. 21 (2010) 2125–2132.
[24] T.J. Webster, C. Ergun, R.H. Doremus, R.W. Siegel, R. Bizios, Enhanced functions of osteoblasts on nanophase ceramics, Biomaterials. 21 (2000) 1803–1810.
[25] G. Wei, P.X. Ma, Nanostructured biomaterials for regeneration, Adv. Funct. Mater. 18 (2008) 3568–3582.
[26] J.J. Videau, V. Dupuis, Phosphates and biomaterials, Eur. J. Solid State Inorg. Chem. 28 (1991) 303–343.
[27] J.P. Zhong, G.P. LaTorre, L.L. Hench, The kinetics of bioactive ceramics part VII: Binding of collagen to hydroxyapatite and bioactive glass, Bioceramics. 7 (1994) 61–66.
[28] Y. Khan, M.J. Yaszemski, A.G. Mikos, C.T. Laurencin, Tissue engineering of bone: material and matrix considerations, J. Bone Jt. Surg. 90 (2008) 36–42.
[29] S. Bose, M. Roy, A. Bandyopadhyay, Recent advances in bone tissue engineering scaffolds, Trends Biotechnol. 30 (2012) 546–554. doi:10.1016/j.tibtech.2012.07.005.
[30] J.-P. Zhong, D.C. Greenspan, Bioglass [r] Surface Reactivity: From In Vitro to In Vivo, in: BIOCERAMICS-CONFERENCE-, 1998: pp. 415–418.
[31] J.D. Rinehart, T.D. Taylor, Y. Tian, R.A. Latour, Real-time dissolution measurement of sized and

unsized calcium phosphate glass fibers, J. Biomed. Mater. Res. Part A. 48 (1999) 833–840.
[32] J.J. Mazer, J. V Walther, Dissolution kinetics of silica glass as a function of pH between 40 and 85 C, J. Non. Cryst. Solids. 170 (1994) 32–45.
[33] R.W. Douglas, T.M.M. EL-SHAMY, Reactions of glasses with aqueous solutions, J. Am. Ceram. Soc. 50 (1967) 1–8.
[34] S.J. Hollister, Porous scaffold design for tissue engineering, Nat. Mater. 4 (2005) 518–524.
[35] D.J. Balazs, K. Triandafillu, P. Wood, Y. Chevolot, C. van Delden, H. Harms, C. Hollenstein, H.J. Mathieu, Inhibition of bacterial adhesion on PVC endotracheal tubes by RF-oxygen glow discharge, sodium hydroxide and silver nitrate treatments, Biomaterials. 25 (2004) 2139–2151.
[36] X. Chatzistavrou, J.C. Fenno, D. Faulk, S. Badylak, T. Kasuga, A.R. Boccaccini, P. Papagerakis, Fabrication and characterization of bioactive and antibacterial composites for dental applications, Acta Biomater. 10 (2014) 3723–3732. doi:10.1016/j.actbio.2014.04.030.
[37] A. Melaiye, W.J. Youngs, Silver and its application as an antimicrobial agent, (2005).
[38] N. Stobie, B. Duffy, D.E. McCormack, J. Colreavy, M. Hidalgo, P. McHale, S.J. Hinder, Prevention of Staphylococcus epidermidis biofilm formation using a low-temperature processed silver-doped phenyltriethoxysilane sol–gel coating, Biomaterials. 29 (2008) 963–969.
[39] K. Glinel, P. Thebault, V. Humblot, C.M. Pradier, T. Jouenne, Antibacterial surfaces developed from bio-inspired approaches, Acta Biomater. 8 (2012) 1670–1684. doi:10.1016/j.actbio.2012.01.011.
[40] J. Hasan, R.J. Crawford, E.P. Ivanova, Antibacterial surfaces: the quest for a new generation of biomaterials, Trends Biotechnol. 31 (2013) 295–304.
[41] N.R. Panyala, E.M. Peña-Méndez, J. Havel, Gold and nano-gold in medicine: overview, toxicology and perspectives., J. Appl. Biomed. (De Gruyter Open). 7 (2009).
[42] G.J. Higby, Gold in medicine, Gold Bull. 15 (1982) 130–140.
[43] P.M. Tiwari, K. Vig, V.A. Dennis, S.R. Singh, Functionalized gold nanoparticles and their biomedical applications, Nanomaterials. 1 (2011) 31–63.
[44] M.-C. Daniel, D. Astruc, Gold nanoparticles: assembly, supramolecular chemistry, quantum-size-related properties, and applications toward biology, catalysis, and nanotechnology, Chem. Rev. 104 (2004) 293–346.
[45] J. Lipka, M. Semmler-Behnke, R.A. Sperling, A. Wenk, S. Takenaka, C. Schleh, T. Kissel, W.J. Parak, W.G. Kreyling, Biodistribution of PEG-modified gold nanoparticles following intratracheal instillation and intravenous injection, Biomaterials. 31 (2010) 6574–6581.
[46] G.L. Semenza, Regulation of Oxygen Homeostasis by Hypoxia-Inducible Factor 1, Physiology. 24 (2009) 97–106. doi:10.1152/physiol.00045.2008.
[47] C. Gérard, L.-J. Bordeleau, J. Barralet, C.J. Doillon, The stimulation of angiogenesis and collagen deposition by copper, Biomaterials. 31 (2010) 824–831.
[48] S. Zhao, L. Li, H. Wang, Y. Zhang, X. Cheng, N. Zhou, M.N. Rahaman, Z. Liu, W. Huang, C. Zhang, Wound dressings composed of copper-doped borate bioactive glass microfibers stimulate angiogenesis and heal full-thickness skin defects in a rodent model, Biomaterials. 53 (2015) 379–391. doi:10.1016/j.biomaterials.2015.02.112.
[49] K. Balamurugan, W. Schaffner, Copper homeostasis in eukaryotes: teetering on a tightrope, Biochim. Biophys. Acta (BBA)-Molecular Cell Res. 1763 (2006) 737–746.
[50] L. Finney, S. Vogt, T. Fukai, D. Glesne, COPPER AND ANGIOGENESIS: UNRAVELLING A RELATIONSHIP KEY TO CANCER PROGRESSION, Clin. Exp. Pharmacol. Physiol. 36 (2009) 88–94. doi:10.1111/j.1440-1681.2008.04969.x.
[51] Y.-J. Park, Y.-H. Song, J.-H. An, H.-J. Song, K.J. Anusavice, Cytocompatibility of pure metals and experimental binary titanium alloys for implant materials, J. Dent. 41 (2013) 1251–1258. doi:10.1016/j.jdent.2013.09.003.
[52] A. Yamamoto, R. Honma, M. Sumita, Cytotoxicity evaluation of 43 metal salts using murine fibroblasts and osteoblastic cells, J. Biomed. Mater. Res. 39 (1998) 331–340. doi:10.1002/(SICI)1097-4636(199802)39:2<331::AID-JBM22>3.0.CO;2-E.
[53] D. Wojcieszak, D. Kaczmarek, A. Antosiak, M. Mazur, Z. Rybak, A. Rusak, M. Osekowska, A. Poniedzialek, A. Gamian, B. Szponar, Influence of Cu–Ti thin film surface properties on antimicrobial activity and viability of living cells, Mater. Sci. Eng. C. 56 (2015) 48–56. doi:http://dx.doi.org/10.1016/j.msec.2015.06.013.
[54] K.Y. Lee, D.J. Mooney, Alginate: Properties and biomedical applications, Prog. Polym. Sci. 37 (2012) 106–126. doi:10.1016/j.progpolymsci.2011.06.003.
[55] J. Venkatesan, I. Bhatnagar, P. Manivasagan, K.-H. Kang, S.-K. Kim, Alginate composites for bone tissue engineering: A review, Int. J. Biol. Macromol. 72 (2015) 269–281. doi:10.1016/j.ijbiomac.2014.07.008.
[56] Y. Qin, Alginate fibers: an overwiew of the production processes and applications in wound

management, Polym. Int. 57 (2008) 171–180. doi:10.1002/pi.
[57] M. Rinaudo, Main properties and current applications of some polysaccharides as biomaterials, Polym. Int. 57 (2008) 397–430.
[58] A.B. Lansdown, M.J. Payne, An evaluation of the local reaction and biodegradation of calcium sodium alginate (Kaltostat) following subcutaneous implantation in the rat., J. R. Coll. Surg. Edinb. 39 (1994) 284–288.
[59] K. Smetana, Cell biology of hydrogels, Biomaterials. 14 (1993) 1046–1050.
[60] A.D. Augst, H.J. Kong, D.J. Mooney, Alginate hydrogels as biomaterials, Macromol. Biosci. 6 (2006) 623–633. doi:10.1002/mabi.200600069.
[61] R.S. Singh, G.K. Saini, J.F. Kennedy, Pullulan: microbial sources, production and applications, Carbohydr. Polym. 73 (2008) 515–531.
[62] R.S. Singh, G.K. Saini, Biosynthesis of pullulan and its applications in food and pharmaceutical industry, in: Microorg. Sustain. Agric. Biotechnol., Springer, 2012: pp. 509–553.
[63] R.S. Singh, N. Kaur, V. Rana, J.F. Kennedy, Recent insights on applications of pullulan in tissue engineering, Carbohydr. Polym. 153 (2016) 455–462. doi:10.1016/j.carbpol.2016.07.118.
[64] D. Kumar, N. Saini, V. Pandit, S. Ali, An insight to pullulan: a biopolymer in pharmaceutical approaches, Int. J. Basic Appl. Sci. 1 (2012) 202–219.
[65] M.R. Rekha, C.P. Sharma, Pullulan as a promising biomaterial for biomedical applications: A perspective, Trends Biomater. Artif. Organs. 20 (2007) 111–116.
[66] M. Chaouat, C. Le Visage, A. Autissier, F. Chaubet, D. Letourneur, The evaluation of a small-diameter polysaccharide-based arterial graft in rats, Biomaterials. 27 (2006) 5546–5553.
[67] S. Lack, V. Dulong, D. Le Cerf, L. Picton, J.F. Argillier, G. Muller, Hydrogels based on pullulan crosslinked with sodium trimetaphosphate (STMP): rheological study, Polym. Bull. 52 (2004) 429–436.
[68] K.I. Shingel, Current knowledge on biosynthesis, biological activity, and chemical modification of the exopolysaccharide, pullulan, Carbohydr. Res. 339 (2004) 447–460.
[69] H. Bae, A.F. Ahari, H. Shin, J.W. Nichol, C.B. Hutson, M. Masaeli, S.-H. Kim, H. Aubin, S. Yamanlar, A. Khademhosseini, Cell-laden microengineered pullulan methacrylate hydrogels promote cell proliferation and 3D cluster formation, Soft Matter. 7 (2011) 1903–1911. doi:10.1039/C0SM00697A.
[70] J.A. Burdick, K.S. Anseth, Photoencapsulation of osteoblasts in injectable RGD-modified PEG hydrogels for bone tissue engineering, Biomaterials. 23 (2002) 4315–4323.
[71] M. Dadsetan, M. Giuliani, F. Wanivenhaus, M.B. Runge, J.E. Charlesworth, M.J. Yaszemski, Incorporation of phosphate group modulates bone cell attachment and differentiation on oligo (polyethylene glycol) fumarate hydrogel, Acta Biomater. 8 (2012) 1430–1439.
[72] C.B. Hutson, J.W. Nichol, H. Aubin, H. Bae, S. Yamanlar, S. Al-Haque, S.T. Koshy, A. Khademhosseini, Synthesis and characterization of tunable poly (ethylene glycol): gelatin methacrylate composite hydrogels, Tissue Eng. Part A. 17 (2011) 1713–1723.
[73] A. Phadke, Y.R. V Shih, S. Varghese, Mineralized Synthetic Matrices as an Instructive Microenvironment for Osteogenic Differentiation of Human Mesenchymal Stem Cells, Macromol. Biosci. 12 (2012) 1022–1032. doi:10.1002/mabi.201100289.
[74] G. Frens, Controlled nucleation for the regulation of the particle size in monodisperse gold suspensions, Nature. 241 (1973) 20–22.
[75] R.M. Day, A.R. Boccaccini, S. Shurey, J.A. Roether, A. Forbes, L.L. Hench, S.M. Gabe, Assessment of polyglycolic acid mesh and bioactive glass for soft-tissue engineering scaffolds, Biomaterials. 25 (2004) 5857–5866. doi:10.1016/j.biomaterials.2004.01.043.
[76] J.J. Blaker, R.M. Day, V. Maquet, A.R. Boccaccini, Novel bioresorbable poly(lactide-co-glycolide) (PLGA) and PLGA/Bioglass((R)) composite tubular foam scaffolds for tissue engineering applications, Adv. Mater. Forum Ii. 455–456 (2004) 415–419. doi:10.4028/www.scientific.net/MSF.455-456.415.
[77] K. Magyari, L. Baia, A. Vulpoi, S. Simon, O. Popescu, V. Simon, Bioactivity evolution of the surface functionalized bioactive glasses, J. Biomed. Mater. Res. Part B Appl. Biomater. 103 (2015) 261–272. doi:10.1002/jbm.b.33203.
[78] L. Baia, D. Muresan, M. Baia, J. Popp, S. Simon, Structural properties of silver nanoclusters-phosphate glass composites, Vib. Spectrosc. 43 (2007) 313–318. doi:10.1016/j.vibspec.2006.03.006.
[79] K. Magyari, R. Stefan, D.C. Vodnar, A. Vulpoi, L. Baia, The silver influence on the structure and antibacterial properties of the bioactive 10B2O3−30Na2O−60P2O2 glass, J. Non. Cryst. Solids. 402 (2014) 182–186. doi:10.1016/j.jnoncrysol.2014.05.033.
[80] Downs RT., The RUFF project: An integrated study of the chemistry c, Raman and infrared spectroscopy of minerals., in: RUFF Proj. An Integr. Study Chem. C, Raman Infrared Spectrosc. Miner. Progr. Abstr. 19th Gen. Meet. Int. Mineral. Assoc. Kobe, Japan, RRUFF ID: R060180. http://rruff.info/general5HA/display5default/R060180., 2006: pp. 3–13. http://rruff.info/general5HA/display5default/R060180.

[81] S. Zhang, C. Du, Z. Wang, X. Han, K. Zhang, L. Liu, Reduced cytotoxicity of silver ions to mammalian cells at high concentration due to the formation of silver chloride, Toxicol. Vitr. 27 (2013) 739–744. doi:10.1016/j.tiv.2012.12.003.
[82] S. Padilla, J. Roman, S. Sánchez-Salcedo, M. Vallet-Regi, Hydroxyapatite/SiO 2–CaO–P 2 O 5 glass materials: In vitro bioactivity and biocompatibility, Acta Biomater. 2 (2006) 331–342.
[83] A. Mechler, A.A.J. Torriero, A. Nafady, C.-Y. Lee, A.M. Bond, A.P. O'Mullane, S.K. Bhargava, The formation of gold nanoparticles using hydroquinone as a reducing agent through a localized pH change upon addition of NaOH to a solution of HAuCl 4, Colloids Surfaces A Physicochem. Eng. Asp. 370 (2010) 35–41.
[84] J. Serra, P. Gonz, FTIR and XPS studies of bioactive silica based glasses, J. Non. Cryst. Solids. 332 (2003) 20–27. doi:10.1016/j.jnoncrysol.2003.09.013.
[85] R. Veres, D.L. Trandafir, K. Magyari, S. Simon, D. Barbos, V. Simon, Gamma irradiation effect on bioactive glasses synthesized with polyethylene-glycol template, Ceram. Int. 42 (2016) 1990–1997.
[86] H. Aguiar, J. Serra, P. González, B. León, Structural study of sol – gel silicate glasses by IR and Raman spectroscopies, J. Non. Cryst. Solids. 355 (2009) 475–480. doi:10.1016/j.jnoncrysol.2009.01.010.
[87] S. Padilla, J. Roman, A. Carenas, M. Vallet-Regı, The influence of the phosphorus content on the bioactivity of sol–gel glass ceramics, Biomaterials. 26 (2005) 475–483.
[88] R.K. Singh, A. Srinivasan, Bioactivity of SiO 2–CaO–P 2 O 5–Na 2 O glasses containing zinc–iron oxide, Appl. Surf. Sci. 256 (2010) 1725–1730.
[89] A. Barth, Infrared spectroscopy of proteins, Biochim. Biophys. Acta - Bioenerg. 1767 (2007) 1073–1101. doi:10.1016/j.bbabio.2007.06.004.
[90] S. Tunc, M.F. Maitz, G. Steiner, L. Vázquez, M.T. Pham, R. Salzer, In situ conformational analysis of fibrinogen adsorbed on Si surfaces, Colloids Surfaces B Biointerfaces. 42 (2005) 219–225.
[91] K. Nakamura, S. Era, Y. Ozaki, M. Sogami, T. Hayashi, M. Murakami, Conformational changes in seventeen cystine disulfide bridges of bovine serum albumin proved by Raman spectroscopy, Febs Lett. 417 (1997) 375–378.
[92] S. Lu, D. Xia, G. Huang, H. Jing, Y. Wang, H. Gu, Concentration effect of gold nanoparticles on proliferation of keratinocytes, Colloids Surfaces B Biointerfaces. 81 (2010) 406–411.
[93] M. Vallet-Regi, C. Victoria Ragel, A.J. Salinas, M. Vallet-Regí, C.V. Ragel, Glasses with Medical Applications, Eur. J. Inorg. Chem. (2003) 1029–1042. doi:10.1002/ejic.200390134.
[94] A. Vulpoi, L. Baia, S. Simon, V. Simon, Silver effect on the structure of SiO2-CaO-P2O5 ternary system, Mater. Sci. Eng. C. 32 (2012) 178–183. doi:10.1016/j.msec.2011.10.015.
[95] I.-H. Lee, H. Yu, N.J. Lakhkar, H.-W. Kim, M.-S. Gong, J.C. Knowles, I.B. Wall, Development, characterisation and biocompatibility testing of a cobalt-containing titanium phosphate-based glass for engineering of vascularized hard tissues, Mater. Sci. Eng. C. 33 (2013) 2104–2112. doi:10.1016/j.msec.2013.01.024.
[96] R.A. Popescu, K. Magyari, R. Stefan, I. Papuc, L. Baia, Structural Particularities of the silver and copper doped SiO2-CaO-P2O5 Based bioactive glasses, Stud. Ubb Phys. 60 (2015) 103–108.
[97] W. Höland, Glass-Ceramics, in: J.R. Jones, A.G. Clare (Eds.), Bio-Glasses, John Wiley & Sons, Ltd, Chichester, UK, 2012: pp. 97–105. doi:10.1002/9781118346457.ch7.
[98] A.S. Ethiraj, D.J. Kang, Synthesis and characterization of CuO nanowires by a simple wet chemical method, Nanoscale Res. Lett. 7 (2012) 70. doi:10.1186/1556-276X-7-70.
[99] L. Bao, S. Yang, X. Luo, J. Lei, Q. Cao, J. Wang, Fabrication and characterization of a novel hydrophobic CaCO3 grafted by hydroxylated poly(vinyl chloride) chains, Appl. Surf. Sci. 357 (2015) 564–572. doi:10.1016/j.apsusc.2015.08.249.
[100] A. Bonici, G. Lusvardi, G. Malavasi, L. Menabue, A. Piva, Synthesis and characterization of bioactive glasses functionalized with Cu nanoparticles and organic molecules, J. Eur. Ceram. Soc. 32 (2012) 2777–2783. doi:10.1016/j.jeurceramsoc.2012.02.058.
[101] A. Thulasiramudu, S. Buddhudu, Optical characterization of Cu2+ ion-doped zinc lead borate glasses, J. Quant. Spectrosc. Radiat. Transf. 97 (2006) 181–194. doi:10.1016/j.jqsrt.2005.04.006.
[102] M.S. Selim, E. Metwalli, Optical and transport properties of thin sheets of CuO-PbO-B2O3 glasses, Mater. Chem. Phys. 78 (2003) 94–98. doi:10.1016/S0254-0584(02)00186-4.
[103] C. Wu, Y. Zhou, M. Xu, P. Han, L. Chen, J. Chang, Y. Xiao, Copper-containing mesoporous bioactive glass scaffolds with multifunctional properties of angiogenesis capacity, osteostimulation and antibacterial activity, Biomaterials. 34 (2013) 422–433. doi:10.1016/j.biomaterials.2012.09.066.
[104] J.M. Andrews, Determination of minimum inhibitory concentrations, J. Antimicrob. Chemother. 48 (2001) 5–16. doi:10.1093/jac/48.suppl_1.5.
[105] Q. Yang, Y. Zhang, M. Liu, M. Ye, Y. Zhang, S. Yao, Study of fibrinogen adsorption on hydroxyapatite and TiO2 surfaces by electrochemical piezoelectric quartz crystal impedance and FTIR–ATR spectroscopy, Anal. Chim. Acta. 597 (2007) 58–66. doi:10.1016/j.aca.2007.06.025.

[106] K. Magyari, L. Baia, O. Popescu, S. Simon, V. Simon, The anchoring of fibrinogen to a bioactive glass investigated by FT-IR spectroscopy, Vib. Spectrosc. 62 (2012) 172–179. doi:10.1016/j.vibspec.2012.04.006.

[107] R.A. Popescu, K. Magyari, A. Vulpoi, D.L. Trandafir, E. Licarete, M. Todea, R. Stefan, C. Voica, D.C. Vodnar, S. Simon, I. Papuc, L. Baia, Bioactive and biocompatible copper containing glass-ceramics with remarkable antibacterial properties and high cell viability designed for future in vivo trials, Biomater. Sci. (2016) 1252–1265. doi:10.1039/c6bm00270f.

[108] S. Saber-Samandari, M. Gazi, Pullulan based porous semi-IPN hydrogel: Synthesis, characterization and its application in the removal of mercury from aqueous solution, J. Taiwan Inst. Chem. Eng. 0 (2015) 1–9. doi:10.1016/j.jtice.2015.01.013.

[109] C. Sartori, D.S. Finch, B. Ralph, Determination of the cation content of alginate thin films by FT-IR spectroscopy, Polymer (Guildf). 38 (1997) 43–51. doi:10.1016/S0032-3861(96)00458-2.